UNIVERSIDADE FEDERAL DO RIO GRANDE DO SUL
INSTITUTO DE FÍSICA
Programa de Pós-Graduação em Física

Propagation of a wavefront shaped by stochastic non-markovian phase patterns *

Amanda Kronhardt Fritsch

Dissertation conducted under the supervision of Professor Dr. Ricardo Rego Bordalo Correia and presented to the Institute of Physics of UFRGS in partial fulfillment of the requirements to obtain the title of Master in Physics.

Porto Alegre
December 2019.

* This study was financed by the Coordenação de Aperfeiçoamento de Pessoal de Nível Superior – Brasil (CAPES) – Finance Code 001.

Agradecimentos

• Sou profundamente grata ao meu orientador, Prof. Dr. Ricardo R. B. Correia, por toda a dedicação e confiança depositadas em mim, pela ampla contribuição ao meu desenvolvimento acadêmico e pessoal sempre com muita leveza e parceria.

• Pelas relevantes conversas que contribuíram para o desenvolvimento deste trabalho sou grata ao Prof. Dr. Cristian Bonatto.

• Agradeço ao meu namorado, Guilherme Lorenzatto Volkmer, cujo o apoio tem sido vital para cada aspecto da minha vida, inclusive na elaboração deste trabalho. Sou imensamente grata por poder dividir a vida contigo.

• Agradeço aos meus pais que por me darem todo o suporte necessário para chegar até aqui sempre fazendo o possível para que eu pudesse alcançar meus objetivos.

• Meus sinceros agradecimentos à Anelite e ao Paulo por me acolherem como uma filha no seio da sua família desde os primeiros anos da graduação, assim como aos meus "irmãos" agregados ao longo destes anos Igor e Renata.

• Por tornarem essa jornada mais divertida e prazerosa, agradeço aos meus colegas de laboratório Vinícius C. Ferreira, Érico Braun e especialmente à minha colega de pesquisa e amiga, Claire M. Cisowski, com a qual eu aprendi muito desde o início e que teve papel fundamental no desenvolvimento deste trabalho.

• Agradeço ainda à CAPES pelo apoio financeiro sem o qual este trabalho não seria possível.

Abstract

We propose the wavefront shaping by a non-markovian phase pattern based on the Fresnel zone plate (FZP) framework. The presented phase pattern was designed to produce a light beam with a null central intensity along the propagation axis, while carrying random non-markovian properties in two dimensions. This work discusses theoretical and experimental results of the intensity profile during the propagation of the modulated beam, as well as the influence of non-markovian memory length on the intensity at the focal plane of the FZP. The probability density function (PDF) for these stochastic cases presented a large deviation from the Rayleigh distribution, expected for a markovian phase distribution. Experimentally, all computed cases are reproduced displaying the phase pattern on a spatial light modulator (SLM), designed considering the resolution of this device and of the acquisition camera. Analyzing the phase profile of the propagating beam after modulation, it can be concluded that the central zero corresponds to a stable optical vortex at this position. The creation and annihilation of numerous optical vortices in the beam profile were also pointed out.

Resumo

Propomos a modulação de frente de onda por um padrão de fase não-markoviano baseado na estrutura de uma placa de zonas de Fresnel (FZP). O padrão de fase apresentado foi concebido a fim de produzir um feixe com centro de intensidade nula ao longo de todo o eixo de propagação, portando propriedades aleatórias não-markovianas em duas dimensões. Este trabalho discute resultados teóricos e experimentais do perfil de intensidade durante a propagação do feixe modulado, bem como a influência da memória não-markoviana na distribuição de intensidade no plano focal da FZP base. A função densidade de probabilidade (PDF) para estes casos estocásticos apresentou um grande desvio da distribuição de Rayleigh, esperada para uma distribuição markoviana de fases, revelando o favorecimento do surgimento de eventos extremos em feixes modulados por este padrão de fase. Experimentalmente, todos os casos computados foram reproduzidos utilizando um modulador espacial de luz (MEL) exibindo o padrão que foi desenvolvido considerando as resoluções deste dispositivo e da câmera de aquisição. Analisando o perfil de fase do feixe propagante após a modulação, conclui-se que o zero central corresponde a um vórtice ótico estável nesta posição. Foram apontadas ainda, a criação e aniquilação de inúmeros vórtices óticos no perfil do feixe.

Index

Introduction

Historically it can be easily verified that optics and its applications has experienced an intense development emerging from the debate of the nature of light. Among the early descriptions are the *corpuscular theory*, proposed by Isaac Newton (1643-1727) in his famous work "Treatise on Opticks", where light is treated as being made of countless tiny bodies emitted by bright objects [1]. In contrast, the physicist Christiaan Huygens (1629-1695) published his own treatise on the subject, arguing that light is an undulatory phenomenon and proposed, at least qualitatively, a propagation mechanism known as the *Huygens' principle* [2]. These contrasting descriptions instigated theoretical and experimental advances aiming to establish the most successful theory to predict light related phenomena [3, 4].

The undulatory nature of light was initially discredited and only acquired notoriety on the late eighteenth century, with further improvements throughout the nineteenth century. The demonstration of the interference phenomenon, allied to the rigorous mathematical foundation introduced through classical electrodynamics, has consolidated the view of light as an undulatory phenomenon of electromagnetic nature. This theory is particularly successful in explaining different optical subjects as diffraction, reflection, refraction, interference, etc. With the advent of quantum mechanics, the old corpuscular theory was revisited [3, 5].

The quantum mechanical formalism has among its pillars the notion that both light and matter particles possess a wave-particle behavior and assign to each particle a wave equation. In the case of light, the duality is manifested through the fact that it exhibits a characteristic particle behavior during the processes of emission and absorption at the same time that it propagates through space as a wave. Usually if a system involves an intense flux of photons and its statistics are not relevant to describe the phenomenon, the quantum nature of light can be neglected and the undulatory properties are dominant. In such regimes the physical optics approach is adopted [5]. This is the case found in phase modulation applications, as presented in this work.

The first chapter reviews some fundamental concepts in the description of light as an electromagnetic wave, as well as some wave properties and its interactions. The chapter culminates with discussions about light propagation in free space using the *Huygens-Fresnel principle* and the construction of Fresnel zones. Lastly the numerical method, adopted for simulating the light propagation, is presented and analyzed by considering the adequate approximations enunciated throughout the chapter.

The second chapter is dedicated to an introduction to a wavefront shaping technique and its impacts on optics from the fundamental level to application development. The chapter also describes the equipment used in this work and how it acts in order to imprint on the beam's wavefront the designed phase pattern. Different areas benefited by the development of such technology are briefly explored and it is also presented some distinguished works connected to the pattern proposed here.

The development of the structure for the phase pattern proposed in this work is presented on the third chapter, as well as how the concepts treated on previous chapters can be applied to the method for the phase distribution throughout the structure. The results for the experimental measurements are exposed on the fourth chapter, confirming the numerical predictions, followed by a statistical analysis of the intensity distribution, showing the effects of the non-markovian memory on the intensity statistics. Finally a glimpse on the phase patern, highlighting the existence of optical vortices in the beams profile, as well as the creation and annihilation of optical vortices during the propagation.

Chapter 1

Light Propagation

Since the ancient Greeks, the nature of light and how it propagates (sometimes questioning even if it propagates at all) has fomented countless debates throughout the history of science. During the seventeenth century the corpuscular theory of light was the preferred view, but alternative proposals based in analogies with water and sound waves started to gain space. Inspired by such ideas Christiaan Huygens formulated his own wave theory of light through an approach that was at the same time insightful and simple [6].

In his treatise on optics the propagation of light is develop through the *Huygens' principle*: Every point on a propagating wavefront serves as the source of spherical secondary wavelets, such that the wavefront at some later time is the envelop of these wavelets, as illustrated in (Fig.1.1) [5, 7].

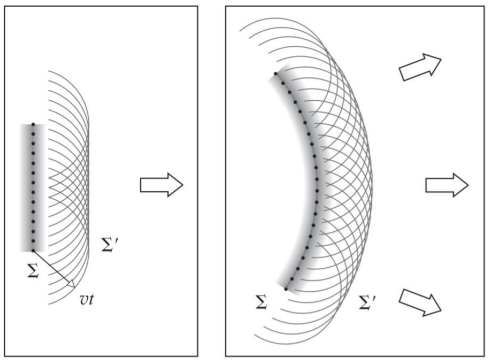

Fig. 1.1: *Illustration of the Huygens' principle for a plane (left) and spherical wave (right) [5].*

Although the Huygens' principle explains relatively well light propagation in free space, it is unable to numerically describe some details of light diffraction. This suggests that, although useful, Huygens' principle needed adaptations to fully describe the propagation of light [3, 5].

In the nineteenth century, the formalization of the electromagnetic theory combined the different equations that describe the behavior of the electric field ($\vec{E}$), as well as the magnetic field ($\vec{B}$) and their interdependence relations. The theory provided a deeper understanding of the nature of light alongside with a more solid mathematical foundation to treat its propagation (including the phenomenon of diffraction). The Maxwell's equations, that provide a description of how the fields $\vec{E}$ e $\vec{B}$ propagate in vacuum, are given by:

$$\vec{\nabla} \cdot \vec{E} = 0 \qquad \vec{\nabla} \times \vec{E} = -\frac{\partial \vec{B}}{\partial t} \tag{1.1}$$

$$\vec{\nabla} \cdot \vec{B} = 0 \qquad \vec{\nabla} \times \vec{B} = \mu_0 \varepsilon_0 \frac{\partial \vec{E}}{\partial t} \tag{1.2}$$

where the constants ε_0 and μ_0 represent, respectively, the electric permittivity and the magnetic permeability in vacuum. By applying the curl to the Maxwell-Faraday equation and then using the well known vector calculus identity $\vec{\nabla} \times (\vec{\nabla}\times) = \vec{\nabla}(\vec{\nabla}\cdot) - \nabla^2$ together with the other Maxwell's equations, one gets:

$$\vec{\nabla} \times (\vec{\nabla} \times \vec{E}) = -\vec{\nabla} \times \frac{\partial \vec{B}}{\partial t} \tag{1.3}$$

$$\vec{\nabla}(\vec{\nabla} \cdot \vec{E}) - \nabla^2 \vec{E} = -\frac{\partial}{\partial t}(\vec{\nabla} \times \vec{B}) \tag{1.4}$$

$$\nabla^2 \vec{E} = \mu_0 \varepsilon_0 \frac{\partial^2 \vec{E}}{\partial t^2}. \tag{1.5}$$

Repeating essentially the same process to the Ampère's circuital law leads to a similar equation for the magnetic field

$$\nabla^2 \vec{B} = \mu_0 \varepsilon_0 \frac{\partial^2 \vec{B}}{\partial t^2}. \tag{1.6}$$

The vectorial approach is the most adequate for dealing with electromagnetic fields since they propagate in three dimensions, however dealing with scalar quantities is considerably simpler than dealing with vectorial quantities. Having this in mind, since each scalar component of both fields obeys the equations (1.5) and (1.6) individually, the *scalar potential theory* was developed. In this approach, the behavior of all components of $\vec{E}$ and $\vec{B}$ is summarized in only one scalar field $U(\mathbf{r}, t)$ that describes the optical propagation of the beam, thus simplifying the treatment of optical phenomena [3], namely

$$\nabla^2 U(\mathbf{r}, t) - \frac{1}{c^2} \frac{\partial^2 U(\mathbf{r}, t)}{\partial t^2} = 0, \tag{1.7}$$

where $c \equiv \frac{1}{\sqrt{\mu_0 \varepsilon_0}}$. Although there are quite a number of limitations, this method allows a faithful description of the intensity pattern generated by a propagating field depending on both space, $\mathbf{r}$, and time, t [3]. So, by looking at the wave equation, it is possible to identify that the electromagnetic field propagates like a wave with velocity $v = c$ in vacuum. Since this observation matches the value

measured for the speed of light, it was crucial to establish the notion of light as an undulatory phenomenon of electromagnetic nature. The solution of the equation (1.7) is a wavefunction, represented by

$$U(\mathbf{r},t) = U_0\, e^{i(\vec{\mathbf{k}}\cdot\vec{\mathbf{r}}-\omega t)}, \tag{1.8}$$

where $\tilde{\mathbf{k}} = k_x\hat{\mathbf{x}} + k_y\hat{\mathbf{y}} + k_z\hat{\mathbf{z}}$ is the *wavevector* that determines the propagation direction of a beam, $\tilde{\mathbf{r}} = x\hat{\mathbf{x}} + y\hat{\mathbf{y}} + z\hat{\mathbf{z}}$ is the position in Cartesian coordinates. There modulus are given by $|\tilde{\mathbf{k}}| = \sqrt{k_x^2 + k_y^2 + k_z^2} = \frac{2\pi}{\lambda}$ and $|\tilde{\mathbf{r}}| = \sqrt{x^2+y^2+z^2}$, respectively. The controlled manipulation of the phase $\phi = \vec{\mathbf{k}}\cdot\vec{\mathbf{r}} - \omega t$ has been used to create beams with a wide range of characteristics, attending the most different needs. This facet will have a central role in this work, as will be presented later.

Independently from Huygens, the physicist Thomas Young (1776-1829) made a valuable contribution to the wave theory of light by demonstrating that, just like matter waves, light exhibits the interference phenomenon, fact that was attributed to the undulatory nature of light [1]. By combining Huygens' concept of wavelets with the interference description made by Young, the french physicist Augustin J. Fresnel (1788-1827) proposed a formalism for light propagation built upon what is now called the *Huygens-Fresnel principle*. This principle states that *every unobstructed point of a wavefront is a source of spherical secondary wavelets with the same frequency as that of the primary wave. The amplitude of the resultant wave at any forward point is the superposition of these wavelets (considering their amplitudes and relative phases).* The Huygens-Fresnel principle was successful in predicting the light diffraction between small openings as well as the bright-dark fringes pattern that results from light diffraction. Taking the limit case where the opening through which light passes is infinite, the Huygens-Fresnel principle can also be used to describe the light behavior when the propagation occurs in free space [3, 5, 7].

[1] Young's double slit experiment, first that demonstrated the interference of light, was elected one of the most beautiful experiments in the history of physics by the magazine Physics World. Besides its importance for classical optics, the experiment is also relevant in quantum physics because the version of the experiment focusing on the particle character was fundamental to elucidate the dual nature of subatomic particles [8].

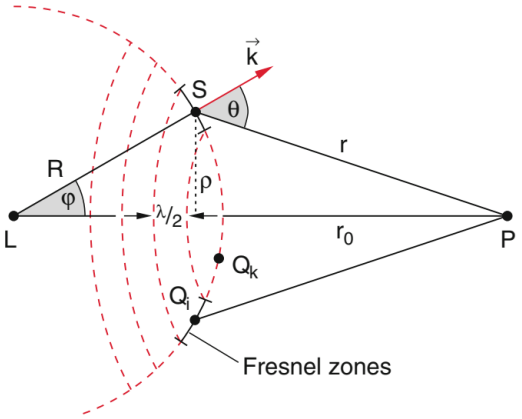

Fig. 1.2: *Fresnel zones construction [9].*

Consider a monochromatic spherical wave [2] emitted by a source at L (Fig. 1.2). The spherical surface of radius R formed by points with same phase is called wavefront. The time periodic factor $e^{-i\omega t}$ being omitted, the optical perturbation at a distance R from the source is given by the scalar field

$$U(R) = \frac{U_0}{R}\, e^{ikR} \tag{1.9}$$

where U_0 is the amplitude of the emitted field [9]. The Huygens-Fresnel principle states that the optical perturbation at the observational point P is the result of the contribution from all wavelets originated at the surface of the wavefront. Let the area element dS of this wavefront be the origin of a secondary wavelet, situated at a point S, its contribution to the optical field at the point P is given by

$$dU(P) = \frac{u_a}{r}\, e^{ik(R+r)}\, K(\theta)\, dS, \tag{1.10}$$

where $u_a = U_0/R$ is the amplitude of the field after propagating for a distance R from the source to S. The field also depends on the distance $\overline{SP} = r$ and on the angle θ between $\vec{r}$ and the wave vector $\vec{k}$ at S, with the last being introduced in the form of the *inclination factor* $K(\theta)$ [7, 9].

The value of $U(P)$ is determined using a specific construction called *Fresnel zones*, which starts by introducing a series of spheres centered in P, with radius $r_1 = r_0 + \lambda/2$, $r_2 = r_0 + \lambda$, $r_3 = r_0 + 3\lambda/2$, ..., $r_m = r_0 + m\lambda/2$ that, when crossing the wavefront around L, divide them in several zones called Fresnel zones. Points at the spherical surface of the wavefront which are at the same distance r from P describe circles with radius $\rho = R\ \sin(\varphi)$ around the central line that connects L and P. The crossing regions between the spheres and the wavefront define the boundaries of the zones, in such a way that for each point Q_i of a Fresnel zone exists a point Q_k in the neighboring zone

[2] Spherical waves are a particular solution of Maxwell's equations in regions far from the sources but near the propagation direction. This is the so called paraxial approximation which is adopted in what follows.

which distance $\overline{Q_kP}$ differs in $\lambda/2$ with respect to $\overline{Q_iP}$. Considering that both R and r are large in relation to the wavelength, the function $K(\theta)$ has a slow variation ($K(\theta) \propto \cos(\theta)$) and can be considered constant inside the Fresnel zone. By applying the cosine law to the LSP triangle the relation $r^2 = R^2 + (R + r_0)^2 - 2R\,(R + r_0)\cos\varphi$ is obtained. Differentiating this expression with respect to φ yields

$$2r\ dr = 2R\,(R + r_0)\sin\varphi\ d\varphi. \tag{1.11}$$

The area element of a Fresnel zone with radius $\rho = R\ \sin(\varphi)$ is given by

$$dS = 2\pi R \cdot R\sin\varphi\ d\varphi. \tag{1.12}$$

Substituting $\sin(\varphi)\mathrm{d}\varphi$ in (1.11), the area element can be rewritten as

$$dS = \frac{2\pi R}{R + r_0} r\ dr. \tag{1.13}$$

Therefore, the contribution from the $m-$th Fresnel zone to the field at P is

$$U_m = K_m \cdot u_a \cdot \frac{2\pi R}{R + r_0} \int_{r_{m-1}}^{r_m} e^{ik(R+r)}\ dr \tag{1.14}$$

$$= -\left[\frac{\lambda K_m u_a R}{i\,(R + r_0)} e^{-ik(R+r)}\right]_{r_{m-1}}^{r_m} \tag{1.15}$$

since $k = 2\pi/\lambda$ and $r_m = r_0 + m\lambda/2$, the equation becomes

$$U_m = (-1)^{m+1}\ \frac{2\lambda K_m u_a R}{i\,(R + r_0)} e^{ik(R+r_0)} \tag{1.16}$$

Note that the contribution alternate its sign between positive and negative for successive zones. This is due to the fact that all points in one zone experience the same phase of the wave emitted by L along all the wavefront. However the optical path length from r to P differs in $\lambda/2$ for point sources in neighboring zones, as determined by the construction of the zones. Therefore this waves are out of phase by π [9]. The resulting field at P can be represented by the sum

$$U(P) = \sum_{m=1}^{N} U_m = |U_1| - |U_2| + |U_3| - |U_4| + \ldots \pm |U_N|. \tag{1.17}$$

Following Fresnel's approach the last relevant zone N has $\theta_{max} = \pi/2$ since all other zones with $m > N$ do not radiate in the direction of the observation point. Using the Schuster's method [7,10], the sum above can be approximated. First (1.17) is conveniently rewritten in the form [7]

$$U(P) = \frac{1}{2}|U_1| + \left(\frac{1}{2}|U_1| - |U_2| + \frac{1}{2}|U_3|\right) + \left(\frac{1}{2}|U_3| - |U_4| + \frac{1}{2}|U_5|\right) + \ldots + \frac{1}{2}|U_N| \tag{1.18}$$

Due to the slow increase of $K(\theta)$ it is possible to approximate that $|U_m| \approx \frac{1}{2}\left(|U_{m-1}| + |U_{m+1}|\right)$ and the terms inside parentheses in (1.18) become negligible, thus the field can be approximated by

$$U(P) \approx \frac{1}{2}\left(|U_1| + |U_N|\right). \tag{1.19}$$

Since the inclination factor has the behavior $K(\theta) \propto \cos(\theta)$, the last zone contribution N is null and $U(P)$ can be approximated by

$$U(P) \approx \frac{1}{2}U_1 = \frac{K_1 \lambda u_a R}{i\,(R + r_0)} e^{ik(R+r_0)}. \tag{1.20}$$

Revealing that the field generated by the totality of the wavefront without obstructions is approximately equal to half of the contribution relative to the first zone [7, 9]. On the other hand, considering a primary wave originated at L and radiating to P gives

$$U(P) = \frac{U_0}{R + r_0}\, e^{ik(R+r_0)}. \tag{1.21}$$

The use of fictitious spheres as a mathematical artifact for developing the description should not change the field at the observation point, therefore comparing (1.21) and (1.20) and remembering that $u_a = U_0/R$ leads to the following expression for K_1

$$K_1 = \frac{i}{\lambda}. \tag{1.22}$$

For the $m-$th Fresnel's zone, $K_m = \frac{i}{\lambda}\,\cos(\theta_m)$. For the first zone $\theta_1 \approx 0 \;\Rightarrow\; \cos(\theta_1) \approx 1$.
Now consider that, for example, the resulting effect in the field at P when an opaque object that has a circular opening, with the size of the first Fresnel zone, is positioned in order to obstruct all zones except the first one. Using (1.16) follows that field is given by

$$U(P) = 2\frac{U_0}{(R + r_0)} e^{ik(R+r_0)}, \tag{1.23}$$

that is, twice as large at P in relation to the unblocked propagation and the intensity ($I(P) \propto |U(P)|^2$) is four times greater at this point! Although it may sound counter intuitive, the statement that a larger opening decreases the field intensity at the point P is not inconsistent, once it is realized that the first two terms in (1.16) have opposite signs and since K_1 and K_2 have very close values, so the reason for the intensity increase is the destructive interference prevention from other Fresnel zones by the opaque object. It can be also verified that an opening with size that encompasses only the two first Fresnel zones furnishes an almost null intensity at P, that is, there is a periodic fluctuation of intensity at P according to the size variation of the opening. A similar result is obtained when both the source and the size opening are held fixed, but the P position varies along the axis [7, 9].

These observations can be explored in order to focus more light at a specific point P than what would be possible with an opening. When the distance R from the opening to the luminous source is much larger that the illuminated opening's diameter, the incident wave can be considered as plane and the Figure's 1.2 imaginary spherical surface becomes a plane containing the Fresnel zones, that assume the form of concentric rings (Fig. 1.3).

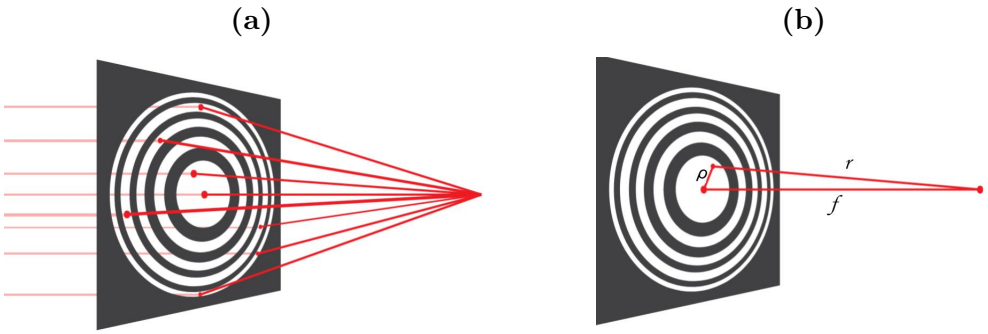

Fig. 1.3: ***(a)*** *Point sources emerge from the FZP and interfere constructively at the focus.* ***(b)*** *Optical path r traveled by a point source. [11].*

In this setting, a secondary source originated at the plate with a radial distance ρ from its center travels an optical path length given by $r = \sqrt{\rho^2 + f^2}$ to a point in a later plane at distance f where the focusing of light at the plate axis is desired. The Fresnel zones construction limits the optical path difference by $\lambda/2$ between secondary sources originated at the same zone, following the same criteria adopted earlier leads to a radius for the $m-$th Fresnel zone given by ${\rho_m}^2 = m\lambda\left(f + \frac{m\lambda}{4}\right)$.

In order to focus light all even zones (or odd) are blocked, thereby the optical path difference between point sources satisfies $(m-1)\frac{\lambda}{2} < r - f < m\lambda$, thus providing only constructive interference. Additionally, the maximum intensity is also predicted by the equation (1.17) once it is noted that all of its members have the same sign [7, 9, 11].

This diffractive device that acts like a lens is known as a Fresnel zone plate (FZP) and its structure has a enormous importance for the scope of this work, as will become evident later. In spite of its simple construction, the FZP has also received attention in X-rays imaging, since it is not possible to use glass (or quartz) refraction in this spectrum region, because these materials absorb X-rays and they have a refraction index $n \approx 1$ in this wavelength range [11].

This diffractive FZP construction does not deplete all power from the source, since already in its construction, on the phase modulation context, the interference that creates the focal point is not reached by blocking the even (or odd) zones anymore. In this approach all light from the source is used and contributes to the interference that is induced by the relative phase control between zones,

that is, besides the acquired phase by the distance difference traveled (ϕ_{path}), the sources at the zones previously blocked now receive a additional phase $\phi_{\text{modulation}} = \pi$,

$$\begin{aligned}\phi_{\text{total}} &= \phi_{\text{path}} + \phi_{\text{modulation}} \\ &= \phi_{\text{path}} + \pi.\end{aligned}$$

The phase difference due the optical path is $0 < \phi_{\text{path}} < \pi$, just like in the diffractive device, with the phase increase given by the modulator the total phase difference becomes $\pi < \phi_{\text{total}} < 2\pi$, producing a constructive interference with greater intensity in comparison with the diffractive FZP. However the focusing efficiency provided by the FZP is also affected by the binary FZP construction presented that, besides the focus, promotes constructive interference points with less intensity at points along the axis with distances given by odd fractions of the focus ($z = f/3, f/5, f/7$, etc). In order to increase the efficiency of the FZP, a variation of this device was developed. It consists in a plate with a phase pattern that varies radially in a smooth sinusoidal way from the axis, generating only one focal point more intense than the binary case, since it acts basically as a hologram of a converging lens [12]. The beam's acquired structure from the phase modulation technique will be approached with more details at the Chapter 3.

1.0.1 Angular spectrum method (ASM)

The Angular Spectrum Method (ASM) will be the method adopted for the numerical calculations of the diffraction patterns found in this work, simulating both intensity and phase profiles of beams modulated by the proposed phase pattern, considering a forward propagation and a paraxial approximation.

The computation of the optical field that propagates to a given plane can be done numerically by many methods, including the direct integration using the equation (1.10). However, the angular spectrum method (ASM) is frequently more convenient and equally accurate, being widely adopted for tracing the optical field in a homogeneous medium [12–15].

The ASM calculates the optical field of a propagating beam in any plane $z = z_0$. Besides calculating the beam's free propagation, the ASM is also used to describe the diffraction suffered by the field that encounter an obstacle, allowing to calculate the intensity and phase profile corresponding to this field. For the purposes of this work this method is interesting for the analysis of the phase profile evolution of the modulated beam.

Consider a monochromatic plane wave propagating through an opening in a transverse opaque plane (x, y), as in (Fig. 1.4). The field at the plane $z = 0$ is described by $U(x, y, 0)$. The wave travels in the positive z direction to a second plane (x', y') at $z = z_0$.

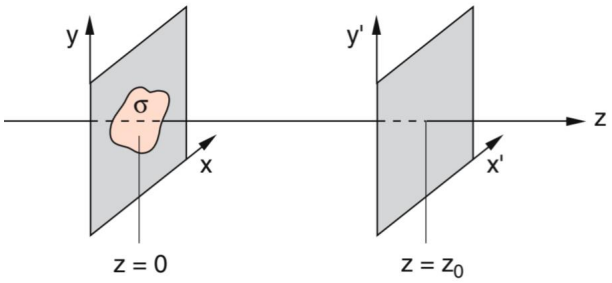

Fig. 1.4: *A monochromatic plane wave focuses on the first plane (x, y), at $z = 0$. The field is modified by the opening σ and $U(x, y, 0)$ travels until it gets to a second plane (x', y'), at $z = z_0$.*

If the complex field distribution of a monochromatic perturbation is analyzed using the Fourier method through any plane, the several Fourier spatial components can be identified as plane waves propagating in different directions away from this plane. The field's amplitude at any other plane can be calculated through the addition of all plane waves, taking into account the changes that each phase suffered [3]. The ASM calculates the optical field at the desired plane with three steps, namely [16]:

- The optical field is taken to the frequency domain:

  The field $U(x, y, 0)$ is rewritten as a sum of two-dimensional plane waves, characterized by the spatial frequencies f_x e f_y

  $$U(x, y, 0) = \iint \mathcal{U}(f_x, f_y; 0) e^{2\pi i(f_x x + f_y y)} df_x df_y \tag{1.24}$$

  The term $\mathcal{U}(f_x, f_y; 0)$ is called *angular spectrum* of the field and is related to it through a two-dimensional Fourier transform ($\mathcal{F}$) at the plane $z = 0$

  $$\mathcal{U}(f_x, f_y; 0) = \mathcal{F}\{U(x, y, 0)\} = \int_{-\infty}^{\infty}\!\!\int U(x, y, 0) e^{-2\pi i(f_x x + f_y y)} dx dy. \tag{1.25}$$

- Each plane wave is propagated to the observation plane:

  Still in the frequency domain the propagation of each plane wave originated at $z = 0$ to the desired plane ($z = z_0$) is calculated. A three-dimensional plane wave in the frequency domain is given by $e^{2\pi i(f_x x + f_y y + f_z z)}$ and in the spatial domain by $e^{i(k_x x + k_y y + k_z z)}$, remembering that $|\vec{\mathbf{k}}| = \sqrt{k_x^2 + k_y^2 + k_z^2} = \frac{2\pi}{\lambda}$, that is, $k_z = \sqrt{\left(\frac{2\pi}{\lambda}\right)^2 - k_x^2 - k_y^2}$. Comparing the plane wave descriptions it can be noticed that they are related through $k_{x,y,z} = 2\pi f_{x,y,z}$.

Finally when the wave propagates to the plane $z_0 > 0$, each plane wave is rewritten using the relation $e^{i(k_x x + k_y y + k_z z)} = e^{2\pi i\left(f_x x + f_y y + z_0\left(\sqrt{\left(\frac{1}{\lambda}\right)^2 - f_x^2 - f_y^2}\right)\right)}$.

- Sum of all propagated waves and return to space domain:

  Adding the contribution from each wave from all points at the plane $z = 0$, the field $z = z_0$ is given by

$$U(x, y, z_0) = \iint \mathcal{U}(f_x, f_y; 0)\, e^{2\pi i\left(f_x x + f_y y + \frac{z_0}{\lambda}\left(\sqrt{1-(\lambda f_x)^2-(\lambda f_y)^2}\right)\right)} df_x df_y \tag{1.26}$$

Briefly, the angular spectrum method can be described in terms of two-dimensional Fourier transforms:

$$U(x, y; z) = \mathcal{F}^{-1}\{\mathcal{F}\{U(x, y; 0)\} \times H(f_x, f_y; z)\}, \tag{1.27}$$

where $H(f_x, f_y; z) = e^{2\pi i\left(f_x x + f_y y + \frac{z_0}{\lambda}\left(\sqrt{1-(\lambda f_x)^2-(\lambda f_y)^2}\right)\right)}$ is the spatial frequency transfer function and $\mathcal{F}^{-1}$ is the inverse Fourier transform [16].

This approach will be implemented numerically using MATLAB software, providing predictions for experimental measurements and allowing testing beyond any experimental limitations. In addition to simulations of intensity and phase profiles, the method will be used as a data source in the following statistical analysis. The appendix A shows the routine that generates our phase pattern and applies the ASM to calculate the propagation of a wavefront modulated by it.

Chapter 2

Structured Beams

Since early times, it is known that by crossing the interface between different media or passing through obstacles and even the incidence over some surfaces changes light's behavior. The interest in these changes has motivated the creation of the first devices for optical manipulation, dating back to centuries B.C. when people used bronze mirrors or magnifying glasses to concentrate sunlight and ignite wood. Such devices change basic light properties like the amplitude, phase, direction and polarization usually induced by the optical phenomena of refraction, reflection, interference and diffraction [17].

Most optical devices exhibit a combination of refractive and diffractive properties, being classified according to the dominant phenomenon, determined by the object's dimensions. In refractive lenses, for example, image parameters are calculated with geometric laws instead of diffractive principles since most of the incident light undergoes refraction and only a small fraction of the incident light needs to be accounted for diffraction in the aperture. However, when the opening is considerably small (comparable to the wavelength), diffraction became the main effect and the device is considered diffractive. The physicist Dennis Gabor (1900-1979) made a crucial step by developing the holography technique, a method to record light's amplitude and phase information of an object, allowing later reproduction of the emitted field through diffraction of a reference beam [18].

Nowadays wavefront shaping has evolved significantly and is used for several purposes. Generally speaking, wavefront shaping can be defined as the process that modifies the electromagnetic field properties in a plane to obtain the desired values in one or more subsequent planes of the propagating beam, enabling the generation of customized optical fields exhibiting wanted characteristics or attending specific needs [17, 19]. The laser was undoubtedly one of the greatest scientific and technological development of the last century. Providing more control of optical characteristics it became an important tool for fundamental research and several applications in a huge variety of

fields, from medicine and biological sciences [20] to optical communication [21], from astronomy [22] and imaging [23] to quantum information [24].

Wavefront shaping provided crucial advances in our knowledge of properties of light, especially from the 1970s that the research and the intense debate about the orbital angular momentum (OAM) of light have attracted much attention to shaping techniques in order to generate these helical beams. Such mobilization is justified by the inherent conceptual richness of these beams that carry a very unique topology with a stable propagating vortex. Furthermore exist a wide range of applications, from imaging and 3D manipulation to classical and quantum communication [19].

The rising experimental interest on these beams during the 1990s boosted the development of devices and methods to generate such beams, among them two stands out, namely, forked grating holograms (Fig. 2.1 a) that encodes the helical phase structure, conferring OAM to a Gaussian beam through diffraction. Another device is the spiral phase plate (SPP), that consists in a disc of transparent material with refractive index n and azimuthally variable thickness. Since an incident plane wave crossing the SPP travels an optical path proportional to the plate thickness, the device is designed to produce a phase difference of $e^{im\phi}$ between portions of the incident beam, converting it to a helical phased beam. This characteristic helical wavefront of these beams, also provide them an interesting central optical vortex (OV) of topological charge m [25].

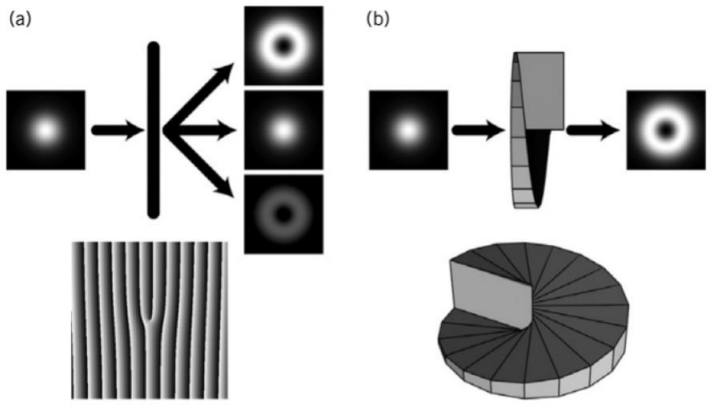

Fig. 2.1: *Two traditional methods to generate OAM beams.* ***(a)*** *Forked hologram, that uses the beam's diffraction and* ***(b)*** *spiral phase plate (SPP), that uses the beam's refraction [25].*

Diffractive devices like holographic plates are traditionally manufactured using photographic emulsions or, more recently, lithograph. Manufacturing traditional refractive devices requires precise equipment to achieve proper curvature and polishing, yet these manufacturing techniques are used to produce devices such as lenses, wave plates and diffraction grids common in any optics laboratory. However, when working with beams carrying more sophisticated structures, the mentioned techniques

can make the manufacturing process extremely laborious, additionally certain applications demand more flexible and tunable devices [3, 11].

In the last decades field mappers allowed for the first time independent and dynamical manipulation of each portion of a wavefront, becoming a key technology for the evolution of researches on structured beams. Spatial light modulators (SLM), devices originally developed for projection systems, are a special class of field mappers that allow real time manipulations of the wavefront using phase patterns or computationally generated holograms without any intermediate manufacturing step, bringing more dynamism and flexibility to light modulation [17, 19].

In devices, the desired phase information is encoded in the controlling part (computer) that sends the adequate stimulation (electric potential variation) to the modulating part, changing its optical properties and resulting in the modulation of the incident light. The electric stimulation sent to the modulating part may alter the phase spatial arrangement, polarization state, intensity profile and direction of propagation of the beam, depending on device construction.[1] [17].

A phase-only SLM, designed to modulate only the beam's phase distribution, usually comprises a liquid crystal layer on a silicon substrate. Liquid crystals are a class of materials that receive their name because they exhibit both liquid (e.g., fluidity) and solid (e.g., crystalline orientation) properties. They are usually composed of rod-shaped organic molecules, such molecular anisotropy affects the material's optical activity, producing birefringence. A birefringent material has two distinct refractive indices: the ordinary (n_o) corresponding to incident light with the electric field polarization state perpendicular to the director vector of the molecule ($\underline{\mathbf{n}}$) and the extraordinary (n_E) for light with polarization state parallel to the same vector, as shown in Fig. 2.2. The effective value for the refractive index is given by $\Delta n = n_E - n_o$ and it is generally positive for liquid crystals [9,27].

Birefringence is the main property of liquid crystals explored by SLMs to manipulate the wavefront shape. The device is constructed accommodating all the liquid crystal molecules aligned in the same direction, so they stay aligned in the absence of an applied electric potential. The circuit responsible for addressing the changes in the applied electric potential is formed by a semiconductor in the silicon layer followed by a layer containing a pixel array formed by electrodes. The electric potential applied to each pixel is controlled independently, so the liquid crystal layer is controlled pixel by pixel (Fig.2.2). When an electric potential is applied the molecules reorient themselves accordingly, the inclination changing of the molecules translates into changing the effective refractive index (Δn)

[1] There is a considerable range of SLM types, here the work is restricted to explain the nematic liquid crystal SLM that changes the beam's phase, adopted in what follows. For more details about other SLM types and variations we recommend [26].

in that region, which changes the optical path length within the liquid crystal layer, causing a phase difference between the beam regions affected by each pixel. A glass substrate keeps the liquid crystal layer at a constant thickness. [27, 28].

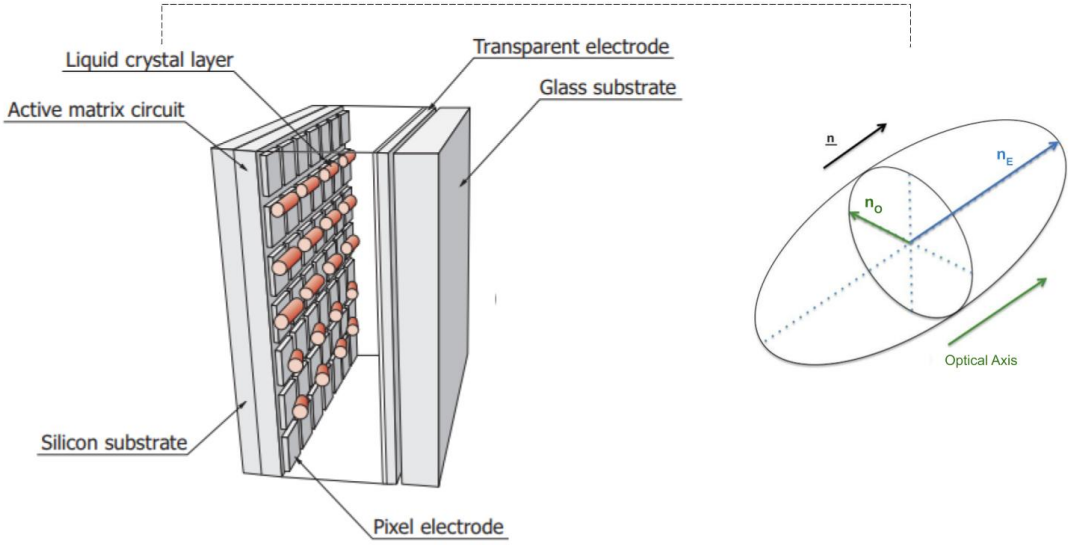

Fig. 2.2: *Components of a reflective SLM. The phase delay conferred by a pixel is determined by the orientation of the liquid crystal molecules in that pixel. These molecules are commonly rod-shaped and birefringent. Figure adapted from [27] and [28].*

The action of the liquid crystal SLMs is conditioned to the beam polarization, so to properly perform wavefront modulation it is necessary that the polarization state of the incident beam is aligned with the orientation of the liquid crystal molecules in the absence of an applied potential.

With a SLM, one can easily reproduce a FZP (or other classical devices) using phase modulation to increase its efficiency by blocking portions of the beam, as described above, but the advantages of a field mapper are not limited to the reproduction of classic devices. Recently, structured beams have been intensely studied, the dynamism and flexibility of this device made possible a great expansion of this field of optical research [19].

In a pioneering experiment, Vellekoop and Mosk [29] demonstrated an impressive control over a random optical field to compensate the scattering of light through a disordered medium. In this experiment, the SLM was used to spatially control the phases of an incident optical field to effectively focus light within a dispersive medium, showing that an adaptive optics approach could be useful even when scattering completely changes the incident field. Since then, many groups have begun to develop iterative wavefront shaping methods. These field optimization methods include

feedback-based wavefront shaping [29–31], transmission matrix measure-based modulation [32–35], optical phase conjugation (OPC) [36–47] and digital OPC (DOPC), which brought even more speed to the focusing process using a guidestar [15] [48]. Light scattering limits many imaging and detection applications, either by altering the waves that carry the image (or information) or by generating background noise. Being able to focus light on scattering media can bring benefits in biomedical applications such as deep tissue imaging, in telecommunications, detection, optical traps and manipulation, optogenetics, etc. [23, 49–57]. The emergence and improvement of adaptive methods was greatly favored by the iterativity and flexibility of SLMs, that brought more control to the generation and optimization of structured light beams. Such versatility also allows to design tunable and more intricate phase patterns without the inherent limitations of a physical device, providing greater reproducibility for both device and its measurements [58, 59].

As the generation and manipulation of beams became more accessible, the interest on the properties, dynamics and applications of OAM beams extended to optical vortices (OV) in general. The study of OVs is actually part of the larger subject of singular optics that has recently gained substantial attention, elucidating that such singularities are not a exclusive of helical beams, in fact they are extremely common features [19, 60].

2.1 Singular Optics

Singularities occur in a wide range of systems, from a storm-generated ocean hurricane to a stress peak in gravitational waves arising from the fusion of two black holes. This type of natural event has relevance in many areas of science, such as chemical and biological systems. Frequently, these events present the formation or annihilation of vortices, given by the flow of a physical quantity around a singular point at which this quantity is not defined [25, 58, 60].

In physics, more specifically in wave systems, the singularities seem to have been first identified by William Whewell (1794-1866) who, by observing the tidal formation in the Nordic Sea, postulated the existence of amphidromic points, that is, points where there is no tide. Tides can be considered as a complex wave function whose wavefronts are the high-tide loci, so a singularity is identified by the radial arrangement of the wavefronts around the amphidromic point, moving away from it [25]. In addition to massive systems, singularities are also present in massless systems such as light. On the ray picture of light propagation, which consider the geometrical optics approach and neglecting the wave nature of light, caustics (i.e. bright surfaces in space on which the light is focused) have been interpreted as singularities [19]. However, in a fundamentally important article considering the wave optics picture, Nye and Berryl demonstrated that even in free propagation an electromagnetic field could carry phase singularities, which they called “dislocations” [61]. The

constant phase lines around this phase singularity describe a spiral in space, so they are usually known as optical vortices [62]. In a way caustics and OVs are complementary singularities, the first has prominent high-intensity features, in contrast to the complete destructive interference that occurs in OVs [19, 58, 60, 63].

As a natural aspect of wave interference, OVs are intrinsic to all sufficiently complex structured light either in random fields from turbulent media or in the simple superposition of three plane waves [64]. Phase singularities can be easily identified as dark spots (or lines in 3D) in the intensity profile featured by various spatial structures [25, 58].

Following this observation, one can recall Young's famous double-slit experiment, which demonstrated the phenomenon of light interference. If Young had opted for a setup with three or more slits, he would have observed a qualitatively different destructive interference phenomenon. In general when three or more waves interfere what is observed in two dimensions is the appearance of dark spots, not fringes. (Fig. 2.3 a and b). A singular point is identified as a point r where the phase $\Phi(r)$ is undefined (singular) and so the intensity (proportional to the amplitude of the optical field $A(r)$) is null at that point. Analyzing the phase in this two-dimensional distribution, we note that in the vicinity of a single point all phase values occur, from 0 to 2π (Fig. 2.3 c and d). This "rotation" endorses the term optical vortex. Since the theory of singular optics has been developed with the support of different areas of mathematics and physics, various terminologies have been aggregated, so in optics various terms are alternately used to refer to optical vortices: singular point, phase singularity or wavefront dislocation, here we use optical vortex [25].

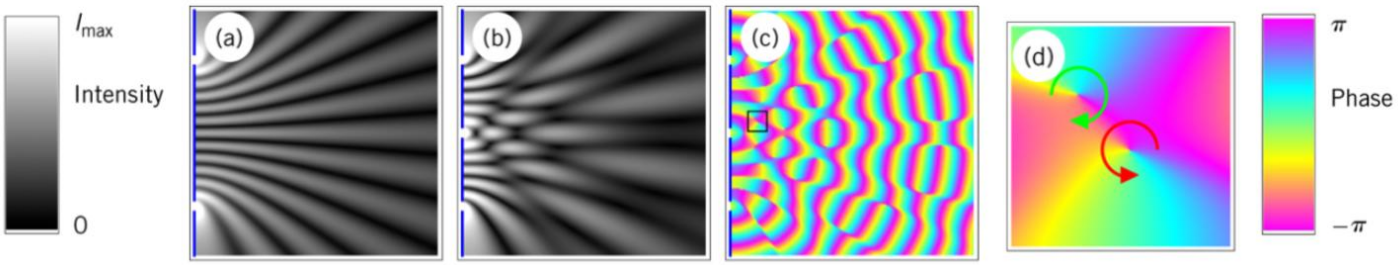

Fig. 2.3: *Two-dimensional representation of the near field in Young's experiment.* ***(a)*** *Diffraction intensity of two slits.* ***(b)*** *Intensity of diffraction by three slits (optical singularities).* ***(c)*** *Phase distribution of (b).* ***(d)*** *Region selected in (c), showing two phase singularities with opposite signs. Figure adapted from [25].*

In addition to dark points in the intensity pattern, an OV can be identified by analyzing the real and imaginary components of the optical field. Consider $f(\mathbf{r}) = \mathrm{Re}\left\{U(\mathbf{r})\right\}$ and $g(\mathbf{r}) = \mathrm{Im}\left\{U(\mathbf{r})\right\}$ of

any optical field $U(\mathbf{r})$, the condition $I(\mathbf{r}) = 0$ is equivalent and can be represented in the form [58]:

$$f(\mathbf{r}) = 0 \quad \text{and} \quad g(\mathbf{r}) = 0. \tag{2.1}$$

Together these conditions imply that phase singularities occur at the intersections of the contours defined by the points where the real part and the imaginary part of the optical field are null. (Fig. 2.4) [58]

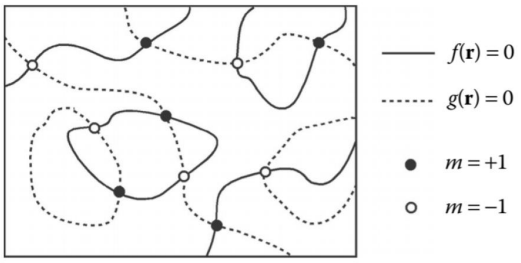

Fig. 2.4: *Contours where the real part $f(\mathbf{r})$ and the imaginary part $g(\mathbf{r})$ of the complex field are null. The optical vortices occur at the intersections [58].*

Regardless of how they were created, optical singularities share a number of common features, so we choose to look at most of these features through a simpler case before moving on to more sophisticated beams. This is the case of Laguerre-Gauss beams, which have a very well defined structure, carry only one central phase singularity. The phase circulation around this vortex implies that Laguerre-Gauss beams naturally carry OAM, making them very popular for fundamental studies and applications of this property of light. The central singularity induces a characteristic *donut*-shaped intensity profile centered on the singularity. The optical field of a Laguerre-Gauss beam can be expressed in cylindrical coordinates (ρ, ϕ, z) by:

$$u_{nm}^{LG}(\mathbf{r}) = \sqrt{\frac{2n!}{\pi w_0^2 (n+|m|)!}} \left(\frac{\sqrt{2}\rho}{w(z)}\right)^{|m|} L_n^{|m|}\left(\frac{2\rho^2}{w^2(z)}\right) e^{im\phi} u_G(\mathbf{r}) e^{-i(2n+|m|)\Phi(z)}, \tag{2.2}$$

where $u_G(\mathbf{r})$ is the field of a Gaussian beam, $\Phi(z)$ is the Gouy shift, $w(z) = w_0\sqrt{1+z^2/z_0^2}$ is the beam waist and $z_0 = \pi w_0^2/\lambda$ is the Rayleigh range. $L_n^m(x)$ is the associated Laguerre polynomial with indices m and n, where n is a positive integer and m is an integer [60]. When $n = 0$, $m = 0$ this expression return the field of a common gaussian beam [25, 58, 60]. Figure 2.5 illustrates how the OV can be identified by the intersection of the the null contours associated with the real and imaginary part of the optical field.

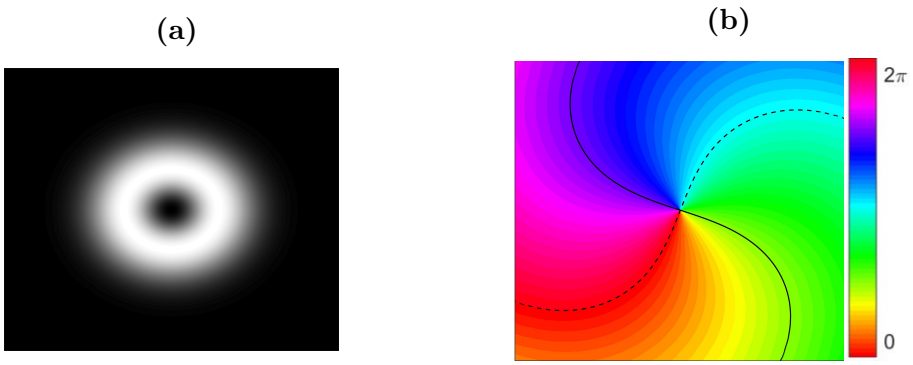

Fig. 2.5: *Intensity* ***(a)*** *and phase profile of a Laguerre-Gaussian beam* ***(b)****, showing the meeting of the curves* $\mathrm{Im}\{U\}$ *(solid line) and* $\mathrm{Re}\{U\}$ *(dashed line) at the singular point.*

An important property of an optical singularity is its topological charge m, it defines the number of times the field cover its entire phase domain within a surface C centered on the singular point:

$$m = \frac{1}{2\pi} \oint_C d\Phi. \tag{2.3}$$

To maintain the continuity of the wavefield, the topological charge of an optical vortex has usually an integer value $m = 0, \pm 1, \pm 2, ...$, being the sign positive or negative depending on whether the phase increases counterclockwise or clockwise, respectively, and if $m = 0$ it means that there is no vortex inside C. The m value is independent of the chosen C curve, as long as the singular point is enclosure and that the curve itself has no singularities. The total topological charge of a beam, given by the sum of the individual charges, is a conserved quantity under smooth perturbations of the wavefield. This important property states that, during the propagation, OVs are typically created and annihilated in pairs of charge with same modulus and opposite sign. This leads to the curious property that for any given vortex in a random field, the topological charge of the nearest neighbor is almost always of the opposite sign. Indeed, higher-order singularities ($i.e. |m| > 1$) are very unstable states and hence unusual in unprepared systems, as they easily decay in vortices with charges equal to ± 1 under minimal changes of the optical field. Conversely, OVs with $m = \pm 1$ can appear naturally in an optical system without any special or conscious preparation, these kind of feature are more robust under slight changes in that system. Such robustness of OVs is one of the most useful properties for many applications of phase singularities [58, 60].

Optical vortices find application over a broad range of systems, from small to great dimensions. An acknowledged imaging technique using OVs is the stimulated emission depletion (STED) super-resolution microscopy. Usually light emitted by a sample is limited by diffraction, STED uses a second illuminating beam, which contain an OV, to suppress almost all the scattered light. The technique allows the observation of small regions of an image by evading the classical optics restriction on size of bright regions (e.g. focal spot), in contrast dark regions can be arbitrarily small. Following

the same principle, the vortex coronagraph is a promising application in which an optical element with a phase vortex diminish the light from a near star, allowing observation of its much fainter planet. Also, the reduced scattering makes singular points with exact intensity nulls (i.e. optical vortices) a useful property for optical trapping of ultracold atoms and Bose–Einstein condensates, for example [19].

Textbook examples, like Young's double-slit experiment or the presented Laguerre-Gauss beam, were conceived to demonstrate and study some properties of light. In these cases interference occurs only between two sources and the phase varies linearly from 0 to $2m\pi$ around the singularity (Fig. 2.5). However, natural interference patterns involve superpositions of a large number of waves as in the scattering from a rough surface. Similarly natural optical singularities are the product of the sum of many waves with different propagation directions, resulting in anisotropic singularities that end up being more common. In an anisotropic vortex the phase variation does not occur uniformly around the singularity, so an anisotropic OV can be understood as the geometric deformation of an isotropic one. As illustrated in figure 2.6, the phase still cover the entire domain around the central vortex, although not uniformly [58].

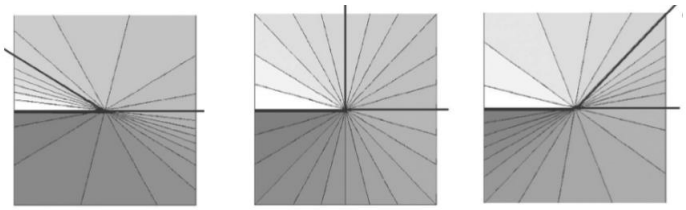

Fig. 2.6: *Examples of two phase distributions for anisotropic vortices (left and right) and the case of an isotropic vortex (center). The lines in this representation stands for a* 15° *phase step [58, 60].*

This type of vortex is featured mainly in disordered fields, being the most common in nature. They can be created when passing through a turbulent or dispersive medium or in the reflection of a coherent beam by a rough surface, for example. A disordered field is generally considered detrimental for imaging or optical information transport, nevertheless, such complex systems can exhibit extraordinary physical properties as optical vortices, that can be used for light confinement or even enabling high resolution imaging techniques. In addition to the numerous applications, these disordered fields known as *speckles* are a valuable source of fundamental research revealing details about the statistical properties of light [65–72], by controlling such properties can dramatically impact the way we view and analyze speckles [73, 74].

2.2 Speckles

Speckle is an extremely complex pattern originated, for example, from the dispersion of a coherent beam by a rough surface, in this scenario each illuminated roughness randomly assigns a phase to the incident beam portion according to surface height fluctuations. The resulting granular structure of the intensity profile consists of a multitude of bright spots (where interference was highly constructive), dark spots (where interference was markedly destructive) and intermediate intensity levels with no obvious relation to the macroscopic properties of the illuminated object (Fig. 2.7 a). Conversely, it seems chaotic and disordered being best described quantitatively by probabilistic and statistical methods [75]. The formation of a speckle is essentially a wave phenomenon, it arises due to the sensitivity of interference on the relative phases of the reflected fields. Looking at the phase profile of a random optical field as a speckle, it shows that dark spots are related to the several vortices exhibited by this type of optical field (Fig. 2.7 b) [25, 60, 73].

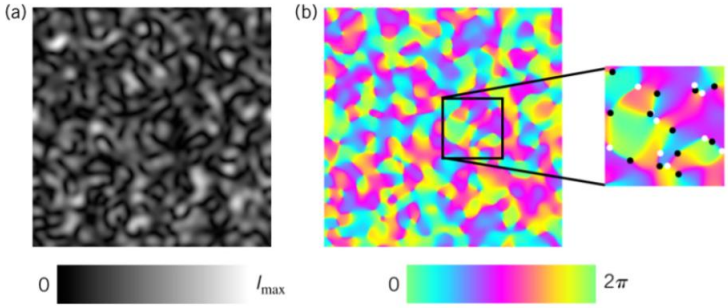

Fig. 2.7: ***(a)****Intensity and* ***(b)*** *phase profile of a speckle. In the selected box are the singular points, in black* $m = +1$ *and white* $m = -1$ *[25].*

Regardless of how they were generated, speckles often present universal statistical properties, known as Rayleigh statistics. The amplitude of a speckle field follows a Rayleigh distribution, constituting a probability density function (PDF) that follows a negative exponential function for the field intensity (I) [60, 73].

$$p(I) = \frac{1}{2\sigma}\, e^{-\frac{I}{2\sigma^2}}, \tag{2.4}$$

where σ is the variance of the intensity values. Regarding the phase distribution, a speckle field is considered fully developed when it has an uniform phase distribution over all possible values. This distribution and the fact that the field is formed by a large number of partial waves with independently variable amplitudes are the reasons that lead the system to follow the Rayleigh distribution [60, 73]. There are cases where a speckle field deviates from this statistic, for example, in the weak scattering regime, where the phase condition is not satisfied, or in the field region near to a dispersive region, where only a small number of waves are detected and relative phases do not cover the entire $[0 - 2\pi]$ domain, a speckle with low contrast emerge and *non-Rayleigh* statistics

take place. Typically *non-Rayleigh* speckles are classified as underdeveloped (when the speckle is the sum of a small amount of waves or when the distribution of the summed wave phases is not entirely random) or partially coherent (sum of incoherent partial waves) [60, 73, 76].

The speckle study raised interest in controlling these statistical characteristics of the optical field, and it has been shown that these properties can be shaped to produce semi-organized intensity patterns [48, 73, 76–78]. For fully developed speckle generation, with a solid *non-Rayleigh* intensity distribution, the interference of a large amount of partial waves whose phases are uniformly distributed over a 2π domain must be considered. Under these conditions it is only possible to generate a *non-Rayleigh* speckle pattern if the complex field associated with the partial waves are statistically dependent [73, 74]. Following this purpose, N. Bender et al. [76] have developed a phase modulation method that allows the generation of fully developed speckles with customized intensity pattern following a pre-established arbitrary PDF. Figure 2.8 presents their results for the intensity patterns and probability density functions (PDF).

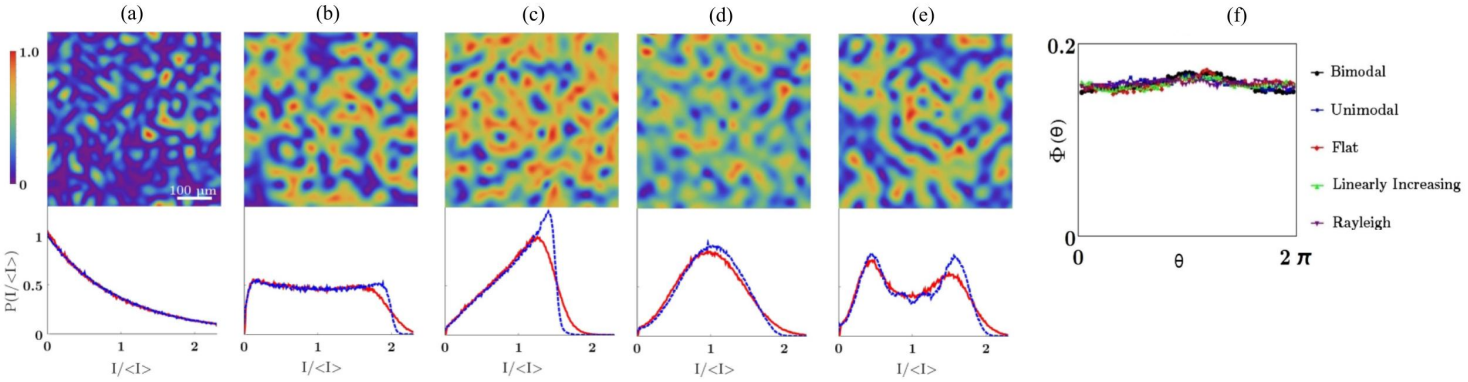

Fig. 2.8: *Intensity pattern and speckle's probability density function (PDF) with statistic* ***(a)*** *Rayleigh (random speckle) and customized with PDF:* ***(b)*** *uniform,* ***(c)*** *linearly increasing,* ***(d)*** *with peak at a nonzero intensity and* ***(e)*** *bimodal. The PDFs, which gather data from 50 independent speckle patterns, the blue line refers to numerically generated patterns and the red line refers to experimental measurements.* ***(f)*** *Phase histogram showing that all generated profiles are fully developed speckles (continuous distribution) [76].*

Intensity distribution customization is widely explored and has a plethora of applications, yet another type of optical field customization that may be of more fundamental interest is the phase imprint of patterns with tailored distributions. Such approach contributes to the understanding of the influence of starting phase distribution on beam propagation and its later characteristics. In this sense, Fischer et al. [78] proposed a wavefront modulation by a stochastic phase pattern that follows a spatially non-markovian distribution, analyzing the effects that the "memory" size between a draw and the previous one has on the resulting intensity pattern in both one-dimensional and two-

dimensional phase patterns. This proposal became known as Sudokulight, since the construction of the two-dimensional phase pattern was based on the quite familiar and naturally non-markovian structure of the sudoku puzzle [79]. In addition to its relevance as the first experimental demonstration of spatially non-markovian light (until then random spatial distributions of phase had been generated exclusively with markovian processes), sudokulight is especially relevant in the scope of this work as it was the inspiration for development of our proposal.

2.2.1 Non-markovian processes and Sudokulight

In 1906, the mathematician Andrey Markov [80] formalized the treatment of an important feature of stochastic systems: how the system *memory* of its previous states affects its future states. He observed that if a system has no memory, the future state of the system can be predicted based on the current state, this property became known as the Markov property (weak condition). The terms "past" and "future" are used because originally the study was dealing with random systems evolving in time, but a stochastic process can also be conceived statically, as a spatial distribution in which the behavior of each member in a markovian system is determined only by the nearest neighbor [81]. Examples of markovian processes are the movement of dust floating in the air or a sequence of simple coin tosses. In the case of a system that has random spatial distribution the simplest example of a markovian process is the traffic jam in which your options as a driver depend only on the car immediately ahead of you, i.e., if it moves slowly, you also move slowly; if it brakes, so must you. However, their decisions are independent of the decisions of all other drivers. As an example of a non-markovian random process, consider a urn containing two red balls and one blue ball. On three consecutive days, a ball is drawn and not returned to the urn. If yesterday a red ball was drawn and today a blue ball, then of course tomorrow a red ball will be drawn. We know this for sure because we take into account the events that affected the state of the urn today and yesterday; that is, tomorrow's draw depends not only on the draw made today but also on past draws [79]. Generally speaking, a non-markovian process can be defined as any process in what previous states have an influence on future states, meaning that it does not present the Markov property. While in a spatially markovian system the members are affected only by the adjacent member, each member of a spatially non-markovian system depends on the behavior of a non-unitary region that can be even the entire system [81].

In nature, most processes are non-markovian, but most of the descriptions of these processes follow markovian models which, due to their simplicity, are often more convenient. However this scenario is changing and recently the interest in characterizing non-markovian evolution of quantum properties in entanglement loss, for example, has become the center of theoretical and experimental efforts, as presented in [82, 83]. These quantum phenomena and their applications are often studied

using optical means, and the controlled generation of entangled quantum states by optical pumping [84] has opened interesting possibilities for modeling desired quantum properties, first in the optical regime and then transferred to other physical systems [85, 86]. Non-markovian light can become a very useful tool for these purposes, and sudokulight was the first beam proposal that carries this property spatially, before that it had only been explored in the temporal domain [78].

In their work the authors imprinted a phase pattern on the beam that corresponds to numerical solutions of overlapping sudoku puzzles, as show on figure 2.9a. They started the process by filling the upper left corner of a SLM with the distributed phase information in the form of a $L \times L$ correctly resolved sudoku, here $L = 9$. They later shifted the frame associated with the sudoku vertically or horizontally by a certain number of cells ($s \leq L$), enlarging the size of the matrix, so some cells retain the previously assigned values while other cells still have an undetermined value. The values assigned to vacant cells were determined following the rules of the sudoku puzzle, that is, integers between 1 and 9 arranged so that they do not repeat either in its row and its column (considering a $L \times L$ sub-matrix). Therefore, the possibilities of values are limited by the $M = L - s$ values preserved from the previous draw, so these portions of the final matrix are correlated by these M values. This measure of the non-markovianity level is called *non-markovian memory*. The process was repeated until all SLM pixels were filled in. After that, the number (n) assigned to each pixel is translated into a phase value given by $\phi = 2\pi\frac{n-1}{L-1}$, ensuring an uniform distribution of L phase values between $0 - 2\pi$. As a result, SLM phase information is stochastic, since the values come from a non-markovian draw, so the information contained in a cell depends not only on the content of the nearest cells, but also on the information contained in the other cells of the corresponding sudoku.

The average intensity pattern of the beams modulated by variations of this phase pattern has a speckle-like intensity profile, differing by the emergence of a low intensity cross-shaped region, reproducing the rectangular geometry of the phase pattern (fig. 2.9b). It was also concluded that the size of this null center decreases as the memory increases, evidencing the influence that the non-markovian property and the memory length imprinted by the phase pattern has on the modulated beam.

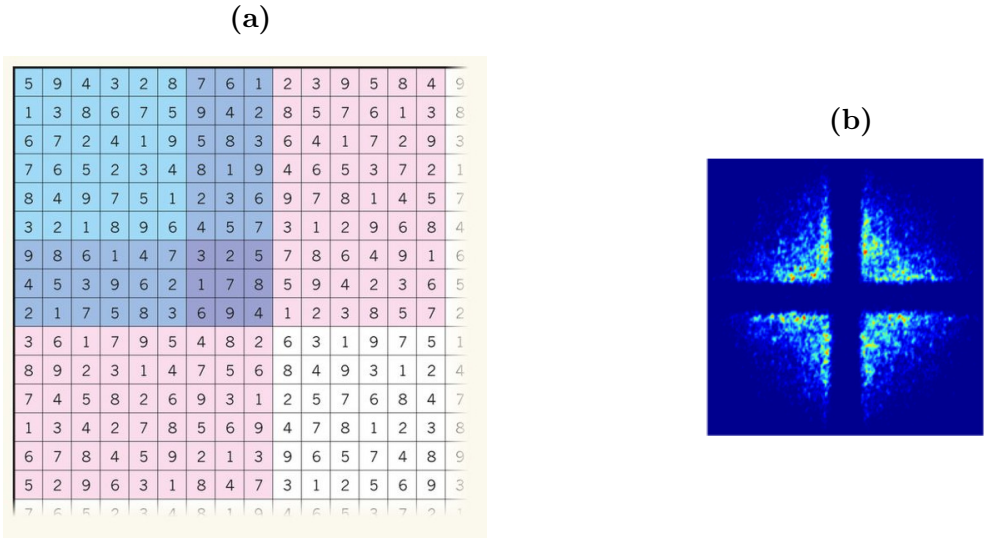

Fig. 2.9: *The creation of sudokulight consists in a wavefront modulation by a spatially non-markovian phase pattern based on overlapping sudokus.* ***(a)*** *The first step in the process of creating this pattern is to place the phase information corresponding to a correctly* 9×9 *solved sudoku (blue). Then the sudoku frame is shifted down (or right) by* s *cells (here* $s = 6$*), forming a new puzzle whose first three elements are already defined. Finally, the empty cells of this second puzzle are filled with values corresponding to a new sudoku solution (pink). This process is repeated until the full SLM matrix is completely filled [79].* ***(b)*** *Average intensity profile of a beam modeled by the pattern described, exhibing the cross-shaped low intensity region [78].*

This modulation proposal carries with it a simplicity that makes it an elegant and productive mean of gaining a deeper understanding of the dynamics of non-markovian processes. The experimental setup with a SLM adds flexibility and ease of reproduction and the combination of control over non-markovian properties with the speed of experimental realization making this approach a cornerstone for experiments targeting specific entangled states.

The sudokulight strongly influenced the purpose of this work. Here we also present a stochastic phase pattern that follows a non-markovian distribution of phase levels in a two-dimensional structure, however our proposal aims to generate a circular null center along the entire propagation axis of the beam as modulated by this phase profile. To ensure these purposes, the phase pattern design was based not only on the above work, but also on the familiar structure of the FZP.

Chapter 3

Stochastic phase pattern designing

Here we present a stochastic phase pattern that follows a non-markovian distribution of phase levels in a two-dimensional structure with cylindrical symmetry. The proposed phase pattern aims to generate a beam with a null intensity center along the *entire* propagation axis, without losing its stochastic characteristic. To make sure that we met these goals, the phase pattern design was based not only on the above-mentioned work, but also on the familiar Fresnel Zone Plate (FZP) structure which, despite having based on trivial physical concepts, is an interesting and useful construction.

3.1 Structure design

The FZP, which underpins this proposal, aims to generate a bright focal point through an entirely constructive interference at the center of a specific plane called the focal plane. In contrast, we want to establish a null center along the entire propagation axis of the beam, so a completely destructive interference is required. Supported by the same premises used for the formulation of the FZP, but with opposite goal, we designed a pattern that has pairs of regions of the same area with canceling phases. These regions are defined by subdividing each zone of a primary FZP into azimuthal sections covering the same azimuthal width, as exemplified by the figure 3.1.

With the established framework, a phase draw is made by ensuring that whenever a phase ϕ is addressed to one section, other section in the same zone has a phase $\phi + \pi$ assigned to it, thus an equal amount of point sources with canceling phases travel given optical path length, leading to a destructive interference. Due to the cylindrical symmetry, the relative angular position of the canceling pairs does not affect the destructive character of the interference and, by repeating it through every zone, further ensures that the center will be null along the entire propagation axis and not only in planes favored by the primary FZP (focal plane and its fractions).

(a)

6	3	2	5	0	8	9	4	7	1
4	9	6	1	5	7	0	8	2	3
7	5	8	9	3	6	1	2	4	0
0	4	9	2	7	1	8	5	3	6
8	0	4	3	1	2	5	7	6	9
9	6	3	7	8	5	4	0	1	2
3	2	1	8	4	0	6	9	5	7
1	7	5	4	6	9	2	3	0	8
2	1	7	0	9	4	3	6	8	5
5	8	0	6	2	3	7	1	9	4

(b)

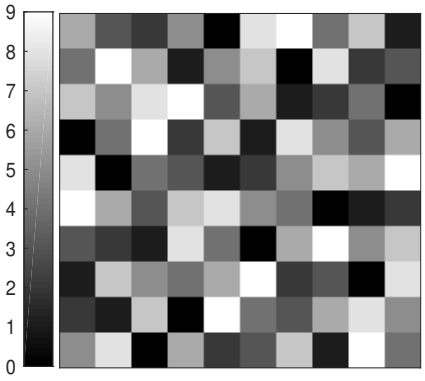

(c)

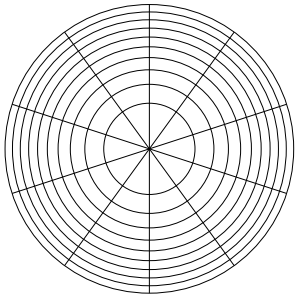

(d)

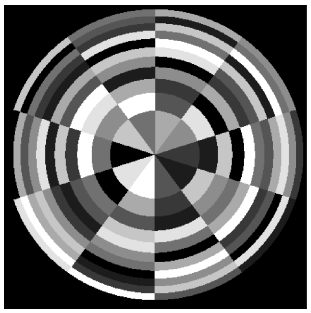

Fig. 3.1: *Creation of the structure of the proposed for a two-dimensional non-markovian phase pattern.* ***(a)*** *First the set of values ($n = 0, 1, 2, ..., 9$) are distributed in a square matrix $L \times L$, ensuring the canceling pairs for each row and each column.* ***(b)*** *Afterwards, a FZP structure with L zones is divided into L azimuthal regions of the same area and later the drawn values are mapped (row, column) $\rightarrow$ (azimuth,zone). Each value drawn corresponds to a grayscale level, as shown in* ***(c)****. Finally this information gives rise to a phase pattern as in* ***(d)****, which will be interpreted by the SLM as a voltage applied to the liquid crystal, imprinting a phase $\phi(n) = n\frac{2\pi}{L}$ on the wavefront of the beam.*

The value assigned to each section is first defined by a matrix that is later mapped to the modified FZP framework, with rows corresponding to radial dimension (zones) and columns corresponding to azimuthal dimension (azimuthal sections). The non-markovian character of the phase pattern is attributed by the way the phases assigned to the sections are drawn. The value of an initial matrix cell is determined by a semi-random draw which, as in sudoku puzzle, that guarantees the same amount of cells with each value in every row and every column. Thus, the draw for one cell restrains the draw of other cells of the same row *and* column, affecting both dimensions. To ensure canceling pairs, the group of possible phase values is predetermined such that it contains uniformly

spaced phases. For example: in a set with $L = 10$ values $n = 0, 1, 2, ..., 9$, each one defines a phase $\phi(n) = n\frac{2\pi}{L}$, where $\phi(n)$ and $\phi(n + \frac{L}{2})$ are canceling pairs. The phase values are converted to an 8-bit grayscale (0-255) that will be interpreted by the SLM as the voltage applied to the liquid crystal molecule. Figure 3.1 clarifies how the primary level matrix ensure non-repeating values in a row/column (as in the sudoku puzzle), showing the design of the proposed framework and finally the translation to phase values and its conformation in the framework.

3.2 Granting non-markovian memory

The non-markovian memory M can be defined as the number of previous states that affect future states. In terms of our problem, the phase assigned to a region depends on the phase drawn for the previous M regions. The $L \times L$ matrix with L phase levels, defined following the rules established in the previous section, represents one execution of the phase draw, so it makes no sense to talk about memory in this configuration. To explore the effects that the non-markovianity of a phase pattern has on the modulated beam, the base matrix for the phase pattern must be larger, in a way that it contains a sufficient amount of draws to consolidate the memory state.

In our proposal, the non-markovian memory is attribute to the pattern through the expansion the initial matrix by coupling at the end of it a random permutation of the initial $s = L - M$ columns, followed by the coupling of the next s columns, and so on (Fig 3.2a). Shifting s columns, the next L continues to display all phase levels only once, keeping the M last values at the same relative position to each other. The same process is repeated independently between the rows of the matrix, so radial memory and azimuthal memory are not necessarily related. (Fig. 3.2b).

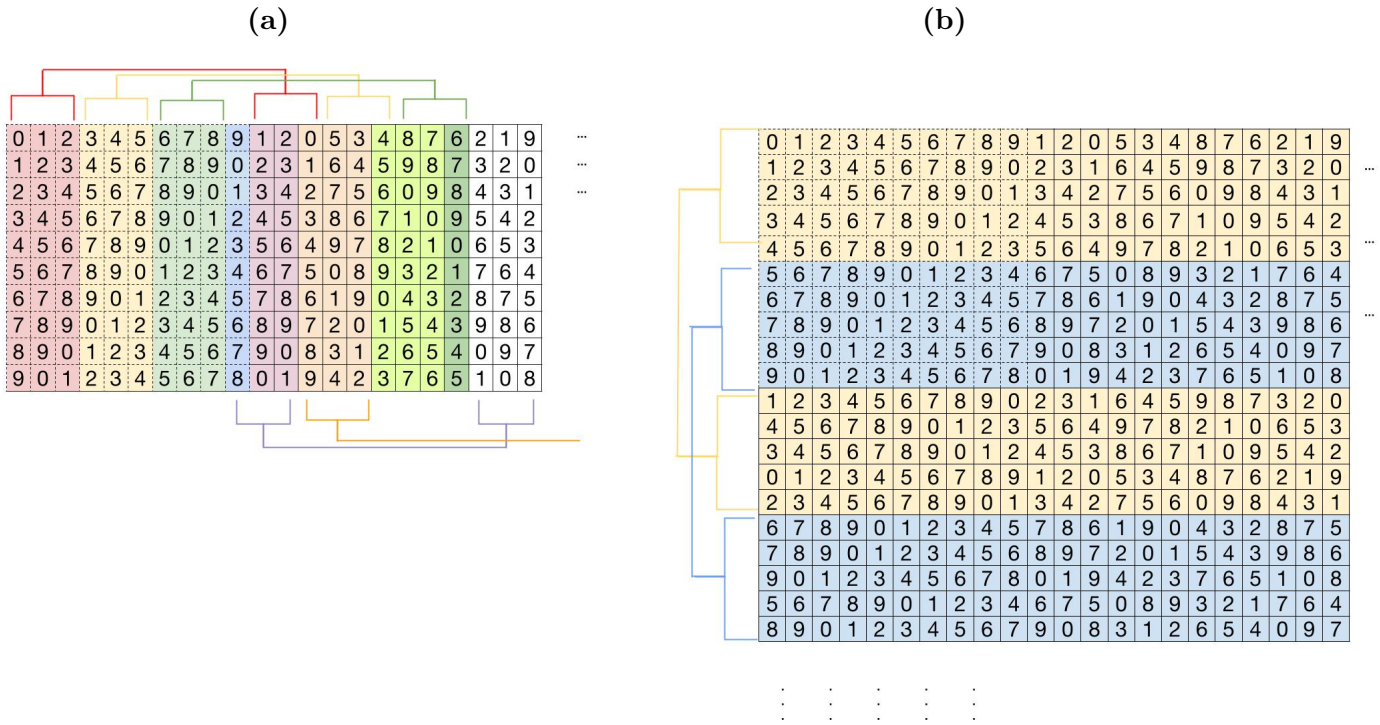

Fig. 3.2: *The primary matrix* 10×10*, represented with dashed borders, expands with the memory defined for each dimension.* ***(a)*** *First step: assigning of a memory* $M_r = 3$ *between columns (zones).* ***(b)*** *Second Step: assigning of a memory* $M_a = 5$ *between rows (azimuthal regions).*

For the case considered in this work, the initial matrix expansion for the memory introduction is limited due to the chosen cylindrical symmetry. The matrix constituting an image is composed of rectangular array of square pixels and the proposed phase pattern has cylindrical symmetry, which causes small distortions in the idealization of azimuthal and zone divisions, however these distortions do not compromise the clarity and functionality of the structure if the size of each region is large enough. To satisfactorily ensure zones and azimuthal sections with sufficient size there is a reasonable maximum number of zones and sections for a given primary FZP focal length. Another factor that determines the final size of the primary matrix is related to the amount of phase levels and the memory length of the draw. Due to the subdivision made when allocating memory to the phase pattern, some memory values require a minimum matrix size to ensure that each phase level is draw with the same amount of elements in a given dimension. This requirement is essential specially to the draw of the elements in the azimuthal dimension, since it is the dimension responsible for generating the null center in the modulated beam, so not all memory lengths guarantee this, considering a limited phase distribution.

Considering these factors and the computational implementation, in this work we have chosen to analyze patterns with 10 uniformly distributed phase levels on the $[0 - 2\pi]$ domain as represented

by phasors in figure 3.3a, assigned in a framework based on a FZP with 1.0 m focal length. Phase patterns with radial memory lengths M_r from 0 to 9 and azimuthal memory lengths of $M_a = 0, 5, 8$ and 9 will be explored, so we opted for a primary matrix with 30 rows (azimuthal sections) and 40 columns (zones), as exemplified in figure 3.3b.

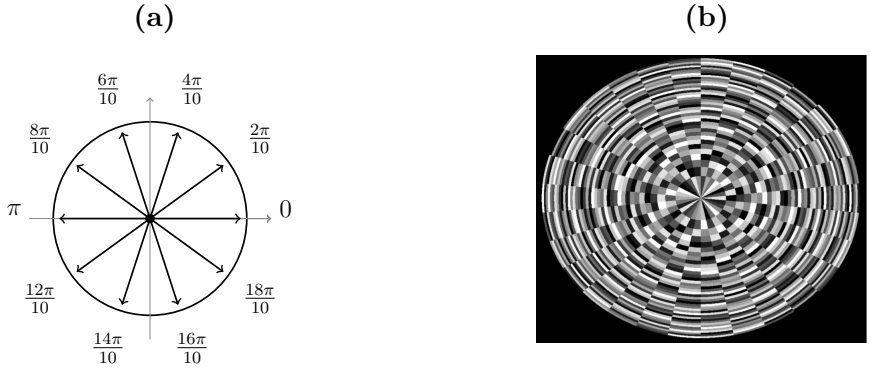

Fig. 3.3: ***(a)*** *Phasor representation of the* 10 *levels distributed in the phase pattern. As every region has the same intensity two phasors with relative phase* π *cancel out, inducing the central zero.* ***(b)*** *An example of a phase pattern analyzed with* 30 *azimuthal sections and* 40 *zones under the structure of a primary FZP with one meter of focal length (not referring to the matrix in Fig. 3.2).*

Observe that a 0 memory draw is not the same as a memoryless (or markovian) draw. In a draw with $M = 0$ and therefore $s = L$, the group of values is entirely permuted at each draw execution, but the execution is still restrained by the no-repeat rule of a element in its row and column. Conversely, a markovian draw can be regarded as a memoryless or completely random draw, that is, the value assigned to each cell in the matrix is independent of everything else.

Regarding the memory length, the correlated phases can be divided into three cases called resonant, quasi-resonant and non-resonant. The case that satisfies the resonance condition typically has a periodic phase distribution, which enhances the coherence property of the waves in the observation plane. The quasi-resonant case occurs when the ratio $L/(L - M)$ is an integer. In this case the phase sequence forms subgroups without common elements and, due to the memory condition, from different subgroups never overlap. For example, in the case $M = 5$ (as in figure 3.2b) there are two subgroups of five random phases and for the case of $M = 8$ there will be five subgroups of two random phases, following this is reasonable conclude that the case $M = 0$ is composed of one group of ten phases. The existence of subgroups decreases the pattern disorder, since it defines the maximum distance between two coherent sources, culminating with the resonant case that can be interpreted as ten groups of one phase each. Finally, non-resonant cases do not establish such a link and the phase pattern presents greater disorder, as in figure 3.2a with memory $M = 3$.

Chapter 4

Modulated beam properties

Describing the effects of our phase pattern on a beam requires a characterization of the intensity profile and phase profile of the modulated beam. Therefore the field was calculated numerically using the ASM method (described in Chapter 1) and implemented with the MATLAB software. Fist of all, a comparison between the numerical predictions and experimental measurements reproducing the same conditions, demonstrate the accuracy of the numerical method. Noticing a good agreement, the simulations were used in a statistical analysis of the beam intensity considering a great number of variations for each memory condition, whose intensity profile were compared aiming to investigate how the memory length in each dimension influence its distribution. The modulated beam, although not random, has speckle-like intensity profile, so the phase profile of the resulting field was also analyzed. Additionally we study the existence of optical vortices especially in the projected null center.

4.1 Intensity Profile

Experimental measurements of the intensity profiles were made with a GaN Fabry-Perot laser diode coupled to a monomode optical fiber and operating at a wavelength of 405 nm. A set of lenses was placed to expand and collimate the incidente beam to a $w = 1.5$ cm waist, illuminating the entire surface of the SLM. In this setup the laser wavefront is modified by a nematic liquid crystal SLM operating in reflective mode, the device has an array of 1280×720 pixels, each squared pixel with $9,5\mu$ m side. The phase pattern is generated by a routine written in MATLAB and the information is sent to the SLM board by a computer through HDMI connection. The reflected beam propagates and the intensity profile is recorded by a CCD camera placed on the desired observation plane (Figure 4.1a).

Previous calibrations indicated that for a wavelength of 405nm, our SLM can only assign phases within the domain $[0-3\pi/2]$. This phase limitation and the device's physical size demand adjustments for patterns in experimental measurements. As the proposal requires pairs of regions with canceling phasors, the phase patterns for experimental measurements are limited to phases in the first and third quadrants of the complex plane, since phases in the second quadrant would be compensated by phases in the fourth quadrant that cannot be achieved. Figure 4.1b shows the phasors for the applied phase levels. Another adaptation is due to the physical dimensions of the device, which limit the size of the framework, since each zone must have a minimum size to not compromise the structure. For the experimental measurements the phase pattern must be based on a FZP with few zones and focal length in the range of a few tens of centimeters. Note that these limitations are not intrinsic to the proposal and a scenery with a full coverage of the phase domain is possible without loss. Experimental results are also limited by the resolution of the acquisition camera as well as the SLM itself, additionally the gaps between each pixel in both devices can brings some side effects, e.g. diffraction, that may affect the precision of the measurements.

By completeness, future numerical analysis in this will consider phase patterns in the domain $[0-2\pi]$. Here experimental measures consider a pattern with 8 phase levels divided into 8 zones and 8 azimuthal sections, based on a FZP with 1.0m focal length.

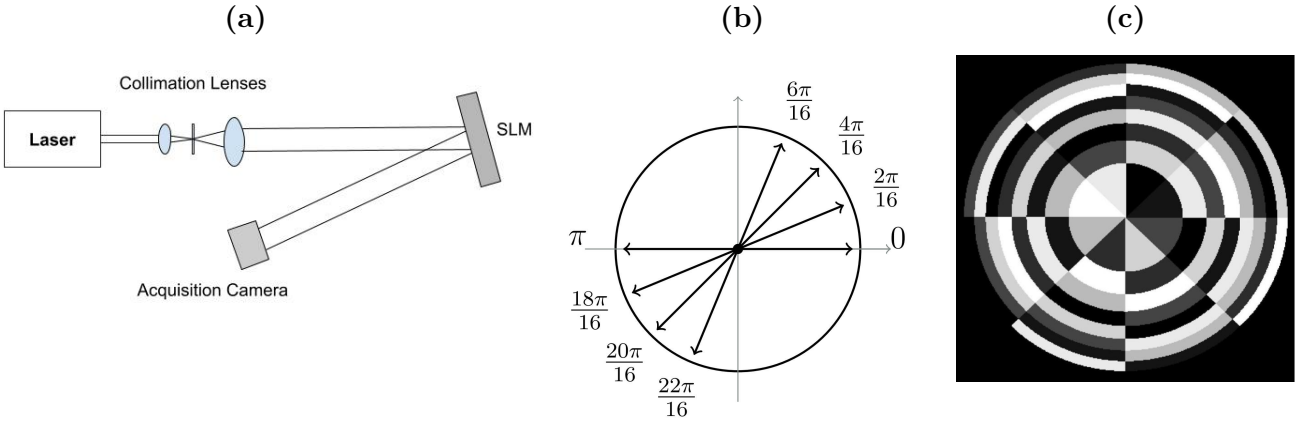

Fig. 4.1: ***(a)*** *Experimental setup.* ***(b)*** *Phasors used in the phase pattern for experimental measurements.* ***(c)*** *Phase pattern with 8 azimuthal regions and 8 zones under the structure of a FZP with a focal length of* $1.0m$.

Figure 4.2 compares the simulated and the measured intensity profile at the focal plane of the primary FZP ($z = 1.0$m). The visual similarity as well as the designed null center is confirmed when looking at the profiles for the central row and column of the image.

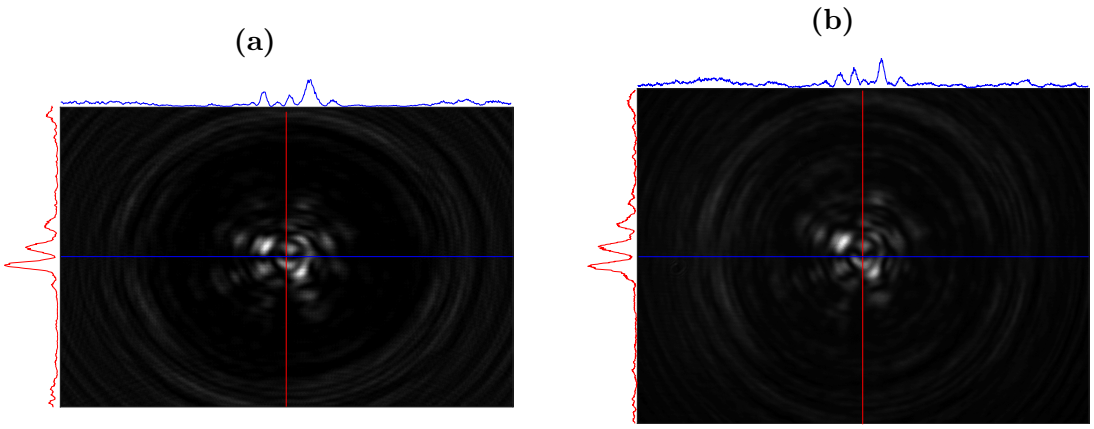

Fig. 4.2: *Comparison between **a)** simulation and **b)** experimental measurement of the beam intensity profile modulated by the phase pattern of the figure 4.1c.*

Figure 4.2 together with figure 4.3, reaffirms the effectiveness of the simulation.

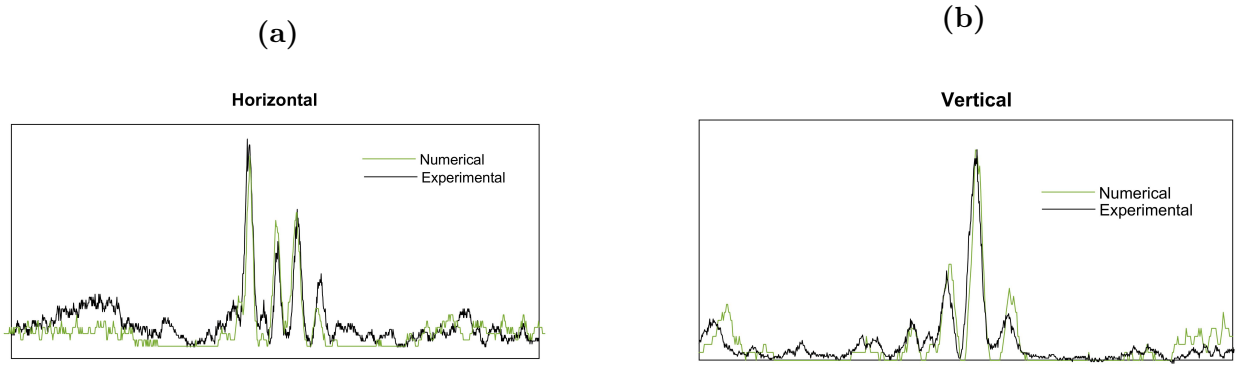

Fig. 4.3: *Comparison between central profiles of the intensity distributions at the focal plane of the FZP-base for experimental and numerical results at **a)** horizontal and **b)** vertical axis.*

In the FZP a constructive interference, even that partially, occurs only in specific plans (z=f, $f/3$, $f/5$...) however, although based on this device, accompanying the propagation of our beam it is noticeable that this phase pattern guarantees a null center along the entire propagation axis, a characteristic visible in both the simulation and the experiment. Even so, the influence of the primary FZP on the intensity profile is not completely lost, along the propagation axis there is a periodic repetition of the intensity structures occurring in these same planes. These aspects are evidenced in the figure 4.4 that compares simulations and experimental measurements of the beam diffraction pattern at three propagation distances: 33.3cm ($f/3$), 50cm ($f/2$) and 1.0m (f). It can be observed constant null center and a similar structure of intensity between profiles at f and $f/3$.

This figure also confirms the effectiveness of the simulation in satisfactorily reproducing the beam intensity profile measured across multiple planes, which gives us greater confidence in exploring configurations that exceed device limitations and draw conclusions based on numerical results. Here we choose to numerically analyze diffraction patterns of the beam at the familiar focal plane of the primary FZP, in the case of this work $z = 1.0$m, as presented in the figure 3.3.

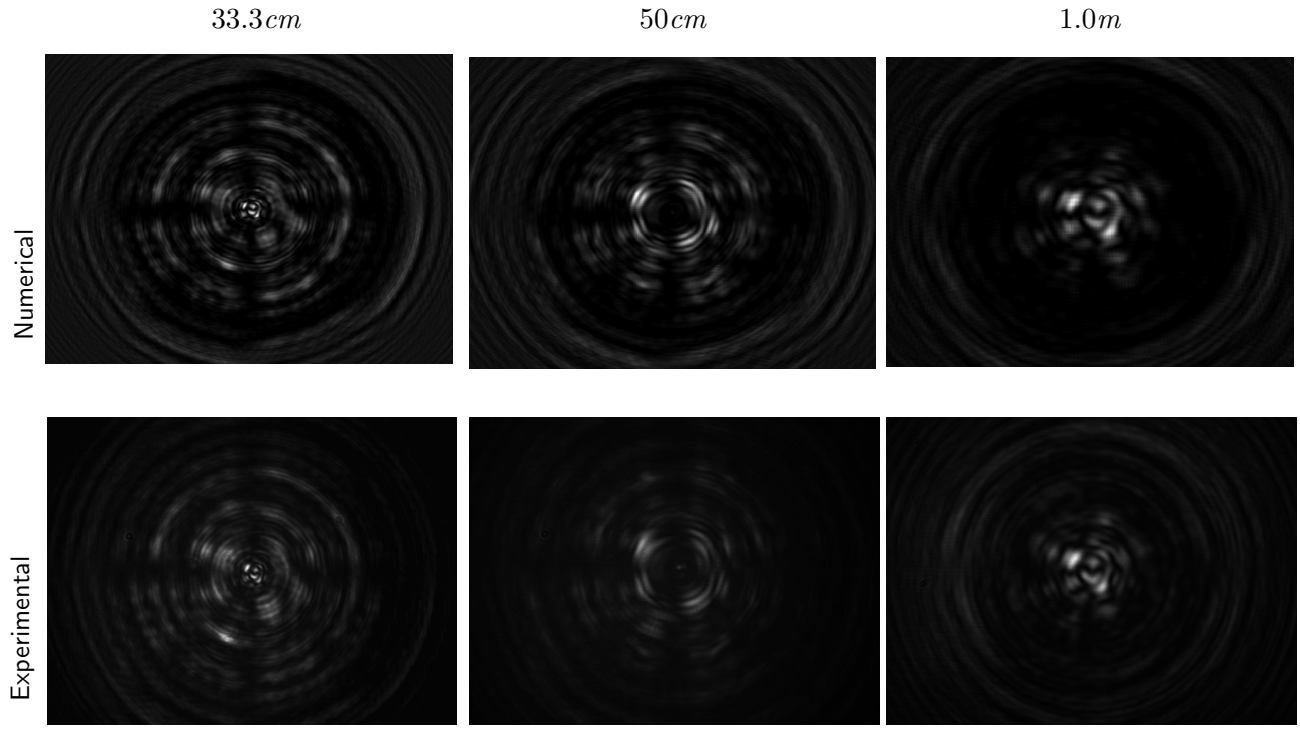

Fig. 4.4: *Comparison between experimental measurements and simulation of propagation distance of* $33.3cm$ *(*$f/3$*),* $50cm$ *(*$f/2$*) and* $1.0m$ *(*f*), respectively.*

Due to the stochastic nature associated with the pattern design, it would be unreasonable to draw conclusions based solely with one realization of each memory state. In order to better analyze the effects of the general characteristic, and not particular ones, of the phase pattern an average of 100 realizations of each memory state was also analyzed. Figure 4.5 shows an example of comparison between average and one realization. The appendix B presents intensity profiles some of the analysed non-markovian memory cases in both dimensions, as well as an average of the corresponding cases. These intensity profiles have a speckle-like intensity profile, differing by their cylindrical symmetry structure and dependence on the radial and/or azimuthal memory of the phase pattern. However, all of azimthally non-markovian draws have the designed null center, a feature that, in general, is more evident looking at the averages.

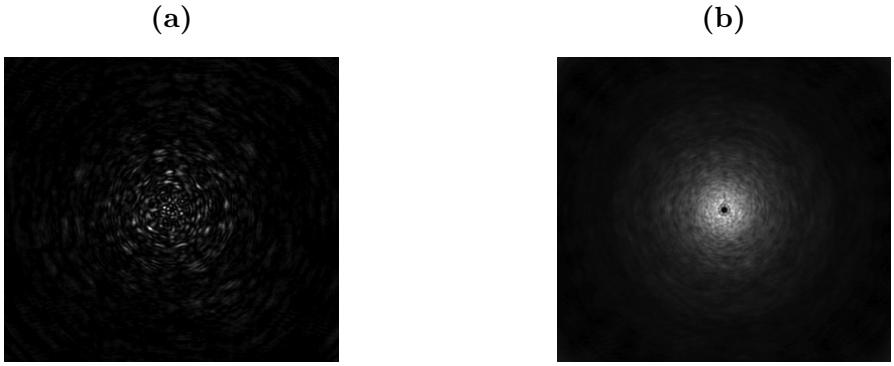

Fig. 4.5: *Comparison between the intensity profile* ***(a)*** *1 realization and* ***(b)*** *the average of 100 realizations. General characteristics, including the null center, are more visible on a average image.*

The influence of the memory length on the intensity profile is noticeable and changes according to the dimension it is presented. To guarantee the null center only quasi-resonant and the resonant value for the azimuthal memory lengths were tested. The numerical results in 4.6 reveals that the phase pattern spoke divisions are still present in the intensity profile, appearing in the form of "petals" of high intensity around the null center. These petals have their size proportional to $s = L - M$, making them almost imperceptible for high memory lengths.

Fig. 4.6: *Comparison between average intensity for cases of* M_r0 *and* ***(a)*** $M_a = 5$ *and* ***(b)*** $M_a = 9$*, pointing the "petal" formation and its size variation depending on* M_a*.*

In the radial dimension the influence of the construction and imprinted memory is clearer. Figure 4.7 shows that the most ordered radial memory case ($M_r = 9$) has an intense light concentration near to the center, while in the extremely disordered case ($M_r =$ markovian) the intensity distribution is more radially uniform. This difference recalls the FZP, where the coherence of the point sources from zones of the same parity induces a constructive interference generating the focal point, for the case $M_r = 9$ coherent point sources are always separated by the same distance from the center of

the phase pattern, inducing a strong constructive interference near the center, however at the center itself destructive interference is induced by the azimuthal distribution of canceling pairs.

Fig. 4.7: *The constructive interference of FZP caused by its periodic feature also induces a constructive interference close to the center at the most ordered radial memory case, being lost as the disorder increase.*

A feature that can be notice comparing the figure 4.2 with the ones at the appendix B, is that the size of the speckle "grain" of the intensity pattern diminish with the size of modulating sections. Taking to the limit case where each section of the phase pattern occupy only one pixel, a characteristic speckle pattern is obtained, as shown in figure 4.8.

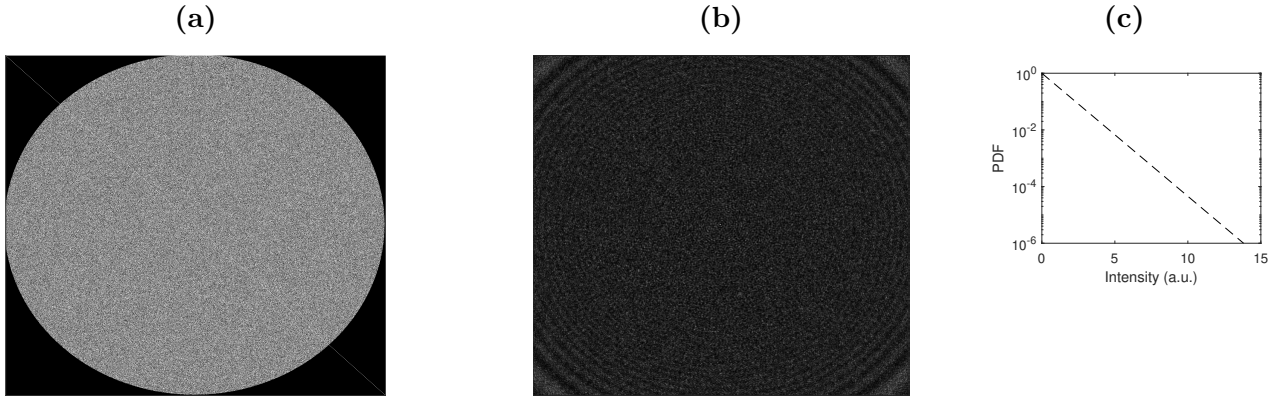

Fig. 4.8: *Phase and intensity profile, respectively, for the limit case where each section occupy only one pixel, highlighting the completely random aspect of this speckle pattern. The probability density function of the intensity distribution follows a negative exponential, typical of the Rayleigh distribution of random patterns.*

4.2 Intensity Statistics

In optics, statistical properties are defining features of light sources. Broadening the description of a beam modulated by our phase pattern, in this section we go into the statistical properties of the intensity distribution.

The figures in the appendix B show that the memory used in the phase draw of the imprinted pattern affects the intensity distribution of the beam in the observation plane, highlighting that an immediate consequence is the variation of the maximum amplitude reached by each memory case. The intensity profiles presented are normalized making the differences in intensity subtle, so only a visual analysis can be very subjective and inappropriate.

To investigate how the memory length influences the emergence of extremely bright spots, we looked at the statistical distribution of intensity values on the observation plane, comparing results between the tested memory lengths in each dimension. For better visualization here will be presented only the PDFs for the case of $M_r = 0$, going through all the azimuthal memory lengths studied, and the case of $M_a = 0$ going through the radial memory cases that represent the general behavior. The conclusions about the behavior of the intensity distribution for these profiles can be extended to the other cases not shown. In addition to the PDFs for the intensity of the cited cases, both graphs present two comparison curves: the first one is a negative exponential that describes the Rayleigh distribution of a random speckle (as in the figure 4.8). The second comparison curve refers to the intensity pattern of 100 beams modulated by a phase pattern with the proposed structure, but whose phases were assigned to each section following the Markov condition in both dimensions. In these two comparison cases the central intensity zero, initially projected in the proposal, is not necessarily present.

Generally speaking, the intensity statistics of the figure 4.9 show that the beams modulated by the proposed pattern have a long tail, that is, high occurrence of pixels with low intensity values and little, but not neglectable, occurrence of very intense pixels. This characteristic distribution indicates that the pattern generates beams with a well-defined structure for all memory cases, including the Markov draw in both dimensions.

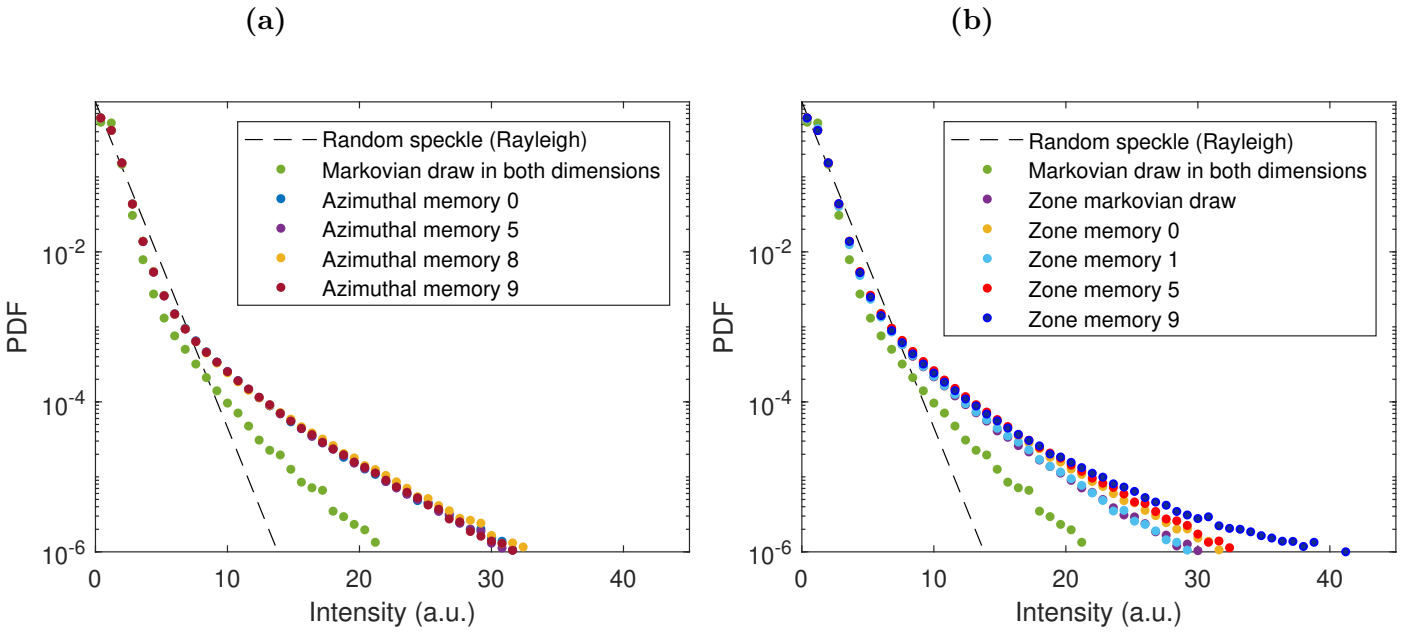

Fig. 4.9: *Probability density function (PDF) of the intensity distribution (in arbitrary units) of the beams modulated by non-Markovian phase patterns.* ***(a)*** *Comparison between different values of M_a, keeping a the radial memory at $M_r = 0$.* ***(b)*** *Comparison between different values of M_r, keeping the azimuthal memory at $M_a = 0$. In both graphs the comparison curves are present. Theses curves refer to the completely random speckle and to the beam modulated with a markovian phase profile in both dimensions, differing from the first since it has a structure of zones and sections.*

Indeed, the emergence of events with high amplitude and low probability is a behavior exhibited by many physical systems. The most established examples are the oceanic "rogue waves", this gigantic waves appears from nowhere and disappears without a trace, but has dramatic impact. The mechanisms behind the arising of oceanic rogue waves are diverse, from linear effects such as directional focusing (as in a lens) or the random superposition of independent wave trains (as seen here), to nonlinear effects associated with the growth of surface noise. Such events are part of a wider theory of extreme events (EE), systems featuring EE can be identified by their characteristic long-tailed distribution of the wave height [87].

Conventional statistical models accounting for describing the height of ocean waves (for example, Gaussian or Rayleigh) suggest that ocean rogue waves should only be observed once in centuries, which contradicts the observations. In fact the height of ocean waves follow a "L-shaped" statistic, i.e., most waves have small amplitudes and high amplitude events far from the median are also observed with low probability, but more frequently than previous models predicted. The first

description of similar instabilities in optics as rogue waves was first made by Solli et al. [88], they reported long-tailed histograms in measurements of intensity fluctuations at long wavelengths in fibre supercontinuum (SC) spectra [87].

In this sense one can conclude that, under this structure, even the most unorganized pattern in the phase draw carries a statistic that surpasses the intensity distribution of a completely random beam. The structure favors the emergence of EE driven by a linear superposition of waves. Although EE occur in all memory cases, the probability depends not only on the memory length, but also on the dimension it is carried. Regarding the influence of the memory length on each dimension, figure 4.9a shows that azimuthal memory alone does not significantly change the probability distribution, reinforcing something that is visible in the intensity profiles. Although it visually influences the intensity profile with its petals, the cylindrical symmetry of the arrangement does not favor greater or less coherence conditioned to the organization of the phase draw.

In contrast, the statistical distribution of intensity is significantly affected by the variation in the radial memory value. Figure 4.9b shows the clear division that exists between non-resonant cases (represented by M_r =markovian and $M_r = 1$), quasi-resonant cases (represented by $M_r = 0$ and $M_r = 5$) and the resonant case ($M_r = 9$). The higher the level of organization, the greater the probability of more intense peaks, culminating in the case of the extremely periodic pattern, that is, with radial memory $L - 1$ (here $M_r = 9$). In the extremely periodic case the optical path length difference between two coherent sources is constant, recalling the periodic relationship proposed by the FZP. In the specific case of even number of levels, the resonant case implies that two coherent sources are always in zones with same parity, justifying the probability increase of more intense peaks.

4.3 Phase Profile

The phase profile of a beam can carry a lot of information about it, so is part of the beam characterization. In this section we will analyze the phase profile of the propagating beam.

Observing the phase distribution of our beam, one can note that the similarities with the speckle are not limited to the granular intensity profile. Just like the random beams, this beam presents uniform phase distribution covering the entire $[0 - 2\pi]$ domain, characteristic of a fully developed speckle. Fig. 4.10 shows the phase distribution for all the memory lengths studied here.

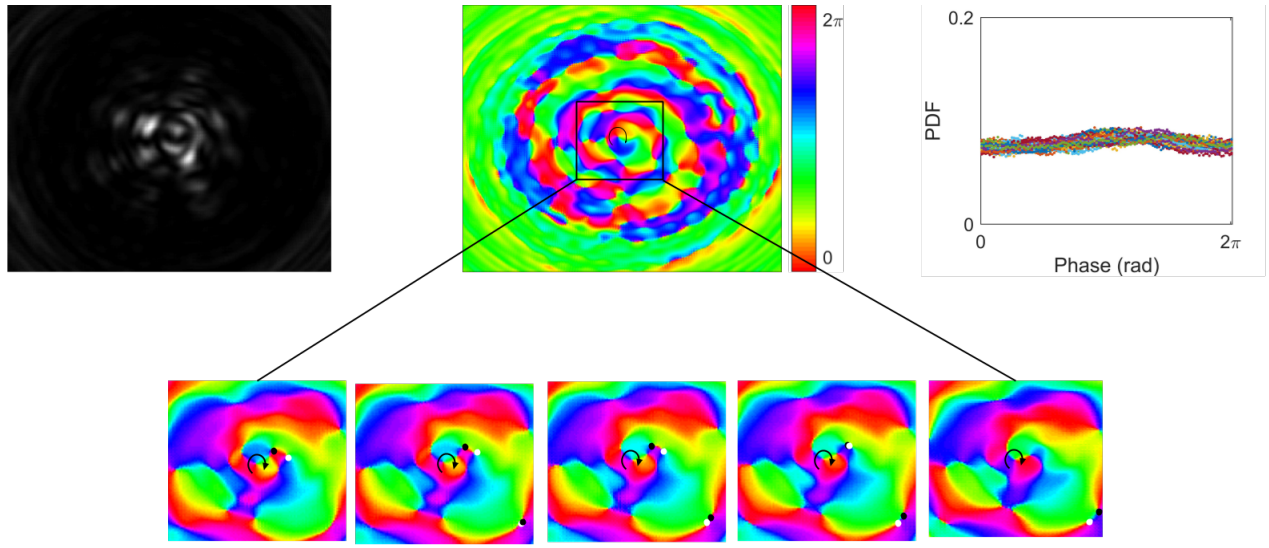

Fig. 4.10: *Intensity and phase profile of the same example of figure 4.2, highlighting the central OV of charge $m = -1$, as well as a pair creation and a pair annihilation of OVs with opposite charge (white dot for $m = 1$ and black dot for $m = -1$) during the propagation, always keeping the central OV. The PDF of phase distribution, showing that these phase profiles are fully developed, i.e., have a uniform distribution.*

In addition to uniform distribution, the phase profile also carries a numerous amount of anisotropic optical vortices carrying topological charges with distinct signs, but with a modulus never greater than 1. These vortices are spontaneously created and annihilated throughout the propagation, as the figure 4.10 exemplifies, always maintaining the total beam charge $m = 0$. Despite such dynamics in propagation, the center with zero intensity is guaranteed by an optical vortex forged by the superposition of waves from all regions of the phase pattern.

4.4 Zone-independent variation

The proposed structure originate beams with a intensity profile presenting a subtle spoke structure connecting the center with the beam edges, it can be removed from the intensity profile with a slight modification in the phase pattern structure. Rotating each zone by a proper random angular factor the connection between one zone and another is destroyed, but within each zone the azimuthal section structure remains and guarantees the central zero (Fig. 4.11a). This variation exemplifies the versatility of the phase pattern.

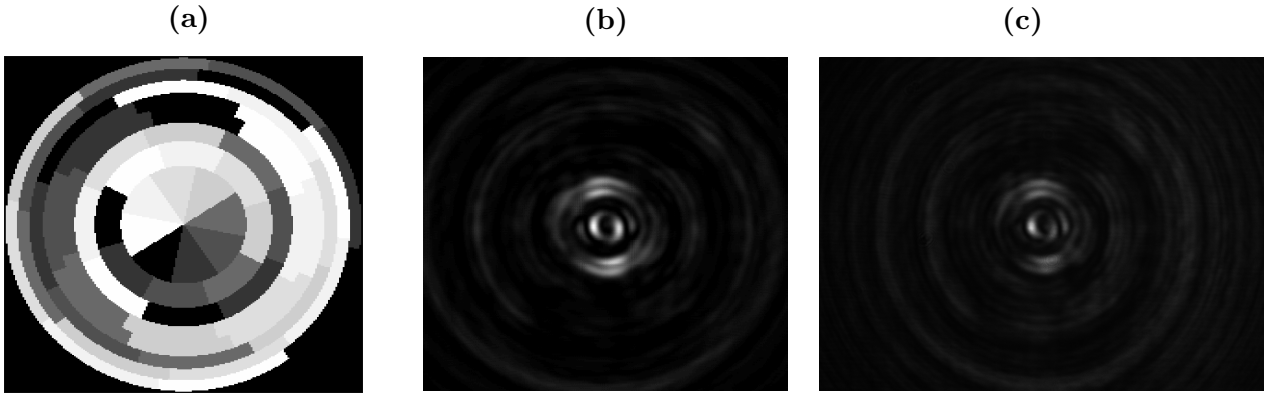

Fig. 4.11: ***(a)*** *Phase pattern without the spoke structure organization.* ***(b)*** *Numerical result for the intensity pattern of a beam modulated by this pattern, showing the smooth intensity variation around the center.* ***(c)*** *Corresponding experimental measurement.*

Concluding Remarks

The structured light and its applications today represent a broad and consolidated area of interest in modern optics and photonics, whose advances extend to biophysics, medical diagnosis, quantum and classical information. The emergence of new modulation techniques has given greater freedom to customize the optical field, enabling the controlled creation of beams with more complex shapes, stimulating creativity and driving development at the fundamental level, but also of numerous interdisciplinary technologies, including optoelectronics, optofluidics, biophotonics and metamaterials. [19].

In this work we proposed a stochastic and spatially non-markovian phase pattern, following the work of Fischer *et al.* [78]. Non-markovian processes and their by-products are very common both in nature and in manufactured devices, even in phase profiles generated in optical elements. The proposal modifies the classic Fresnel Zone Plate (FZP) and, using the same principles, projects the generation of a zero center along the entire axis of propagation of the modulated beam. The characterization of the beam intensity profile modulated by this phase pattern, confirming the generation of the null center, was first made from the numerical calculation of the beam propagation that had its results compared with the experimental results. Since a good agreement was observed between the results, we followed the rest of the analysis with only numerical data, free of experimental limitations.

Evaluating the influence of the non-markovian memory on the beam, it is observed that the intensity profile varies according to the dimension that exhibits the memory, not only with its length. The statistical study comparing different memory cases reveals that the radial order determines the intensity distribution, however in order to generate a null center, the azimuthal condition of cancellation is the fundamental one. This study also showed that the phase patterns developed in this work favor the emergence of more intense points in the observation plane, providing a general picture of how this linear stochastic process favors the emergence of extreme optical events.

There are still possible advances to establish stronger relationships between non-markovian memory and the emergence of extreme events. Since the structure of the FZP favors the centralization of intensity, future works will take into account not only the intensity of the event, but also the distance from the center that it occurs, establishing more directly the relationship with memory length alone. Another point to be optimized is the analysis with larger phase patterns, in a 30×40 matrix with 10 symbols the relation of the memory length is still very modest since this setting does not provide enough repetitions to solidly establish the memory condition in some cases.

The phase profile analysis showed that the success in generating this zero intensity along the propagation is due to the formation of an optical vortex in the central axis, originated from the superposition of many waves with canceling phases. Vortices are formations present everywhere in nature and intrinsic to any optical field with a more sophisticated structure. These circular perturbations can be found in small scale, quantum mechanics, terrestrial scale in gas and liquid turbulence, and even cosmological scale in spiral galaxies. Indeed analogy can be a powerful principle in the visualization connections between distant physical phenomena, and optical vortices can still be protagonists in deeper connections among these areas.

Appendix A

MATLAB routine

Here we present the routine used to generate the non-markovian phase pattern granting non-markovian memory to it. It calculates 100 realizations for each memory case and was developed with our group using the software MATLAB. This routine also evaluates the complex optical field and the intensity profile at a desired plane (denoted by z). In the following code the lines from 8 to 12 generate a $L \times L$ matrix without repeating values in each matrix row and column and lines from 14 to 30 randomize these matrix rows and columns. Lines from 32 to 42 grant non-markovian memory to each dimension. From 54 to 69 the structure proposed for the phase pattern is generated and, finally, from 71 to the end the ASM is applied and the intensity profile is calculated.

```
1 L=10; zonas=40; ang=30; %phase values, number of zones and number of angular sections
2 for k=1:1:4
3 aa=[1,2,5,10]; %only resonant values to generate null center
4 mm=aa(k); % L-mm is the azimuthal memory
5 for m=1:1:L % L-m is the zone memory. We consider all phase levels
6 for g=1:100 %100 iterations for each memory case
7 %*******Generation of a matrix with non repeating elements in each dimension
8 A1=zeros(L,L);
9 A0=randperm(L);
10 for mo=1:L
11 A1(mo,1:L)=circshift(A0,mo-1);
12 end
13 %*******Randomizing the rows and columns to generate the initial matrix*******
14 R=A1;
15 [na, nz]=size(R);
16 for i = 1:na
```

```
swap1 = randi(na);
swap2 = randi(na);
temp = R(swap1,:);
R(swap1,:) = R(swap2,:);
R(swap2,:) = temp;
end
R=transpose(R);
for i = 1:nz
swap1 = randi(nz);
swap2 = randi(nz);
temp = R(swap1,:);
R(swap1,:) = R(swap2,:);
R(swap2,:) = temp;
end
%*******Granting non-markovian memory (m) in zones*******
for n=0:((zonas-L)/m-1)
A=randperm(m);
B=R(:,A+n*m);
R=[R(:,:),B];
end
%*******Granting non-markovian memory (mm) in azimuthal sections*******
for nn=0:((ang-L)/mm-1)
A=randperm(mm);
BB=R(A+nn*mm,:);
R=[R(:,:);BB];
end
%*******Defining variables**********
[Na, Nz]=size(R); %size of the rectangular matrix that will be mapped
lambda= 0.405/9.5; %wavelength in pixels
f = 1000000/9.5; %focal plane of the FZP-base in pixels
z = f; %plane where the intensity will be considered
Ro= 2200; Co= 2200; %size of the image
i = Ro; j = Co;
x = 1:1:i; y = 1:1:j;
freqx = (-1/2:1/(i):1/2-1/(i)); %f_x
freqy = (-1/2:1/(j):1/2-1/(j)); %f_y
%*******Structure with zones and angular sections**********
```

```
54 zz = @(x,y) (((x-(Ro)/2))+1i*((y-(Co)/2)));
55 angulo=2*pi/Na;
56 Phase = zeros(Ro, Co);
57 for u = 1:Ro
58 for v = 1:Co
59 ss = floor(abs(2*(sqrt((f^2)+(zz(u,v))^2)-f)/lambda));
60 tt = 1 + abs(floor((pi+angle(zz(u,v)))/angulo));
61 if ss>=Nz
62 Phase(u,v)=0;
63 else
64 ww = 1 + ss - Nz*floor(ss/Nz);
65 yy = 1 + tt - Na*floor(tt/Na);
66 Phase(u,v)=R(yy,ww)-1;
67 end
68 end
69 end
70 %*****************Propagation***********************
71 parfor nx=1:i
72 for ny=1:j
73 %Transfer function:
74 H12(nx,ny)=exp(1i*2*pi*(z/lambda)*sqrt(1-(lambda*freqx(nx))^2-(lambda*freqy(ny))^2));
75 %Inicial field:
76 u1(nx,ny)=exp((1i*Phase(nx,ny)*2*pi/L));
77 end
78 end
79 % bidimensional Fourier transform leading the field to frequency domain:
80 az1=(fftshift(fft2(u1)));
81 % product with transfer function:
82 az2=az1.*H12;
83 % bidimensional inverse Fourier transform returning the field to space domain:
84 u2=ifft2(fftshift(az2));
85 % squared modulus of the field:
86 Int=(u2.*conj(u2));
87 I(:,:,g) = Int;
88 end
89 end
90 end
```

Appendix B

Numerical results

This appendix presents the numerical calculation for the intensity profiles of a beam resulting from the modulation of a plane wave by the proposed phase pattern. This profiles have normalized intensity levels and correspond to the focal plane of the primary FZP ($z = 1.0$m).

1. Markovian versus non-markovian cases

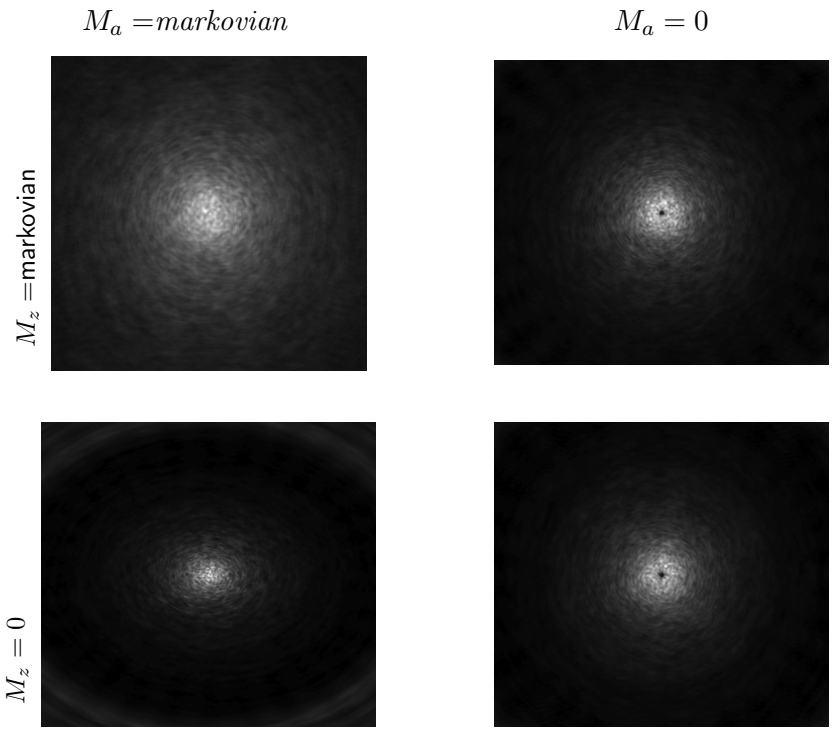

Fig. B.1: *The average intensity profile of* 100 *realization for draws with* $M_z = 0$ *and* $M_a = 0$ *representing non-markovian cases, and* M_z =*markovian and* M_a =*markovian. Comparing these intensity profiles its clear that a non-markovian draw in the azimuthal dimension is essential for a central null intensity.*

2. Non-markovian memory cases for both dimensions (average over 100 realizations)

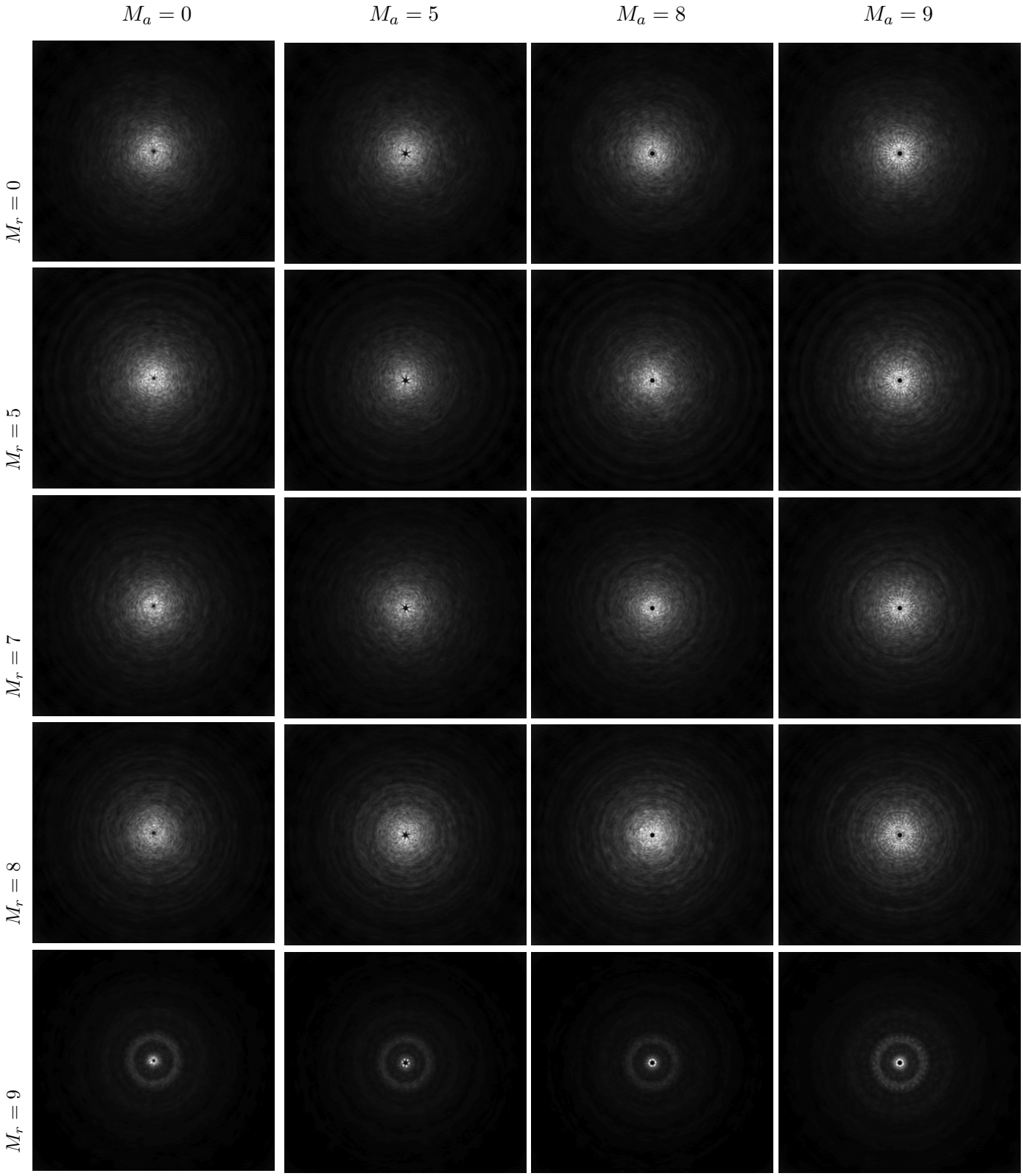

Fig. B.2: *Average intensity profile over* 100 *realizations for all studied azimuthal memory lengths and* $M_a = 0, 5, 8, 9$ *some representative cases of radial memory length* $M_z = 0, 3, 5, 8, 9$.

3. Non-markovian memory cases for both dimensions (1 realization)

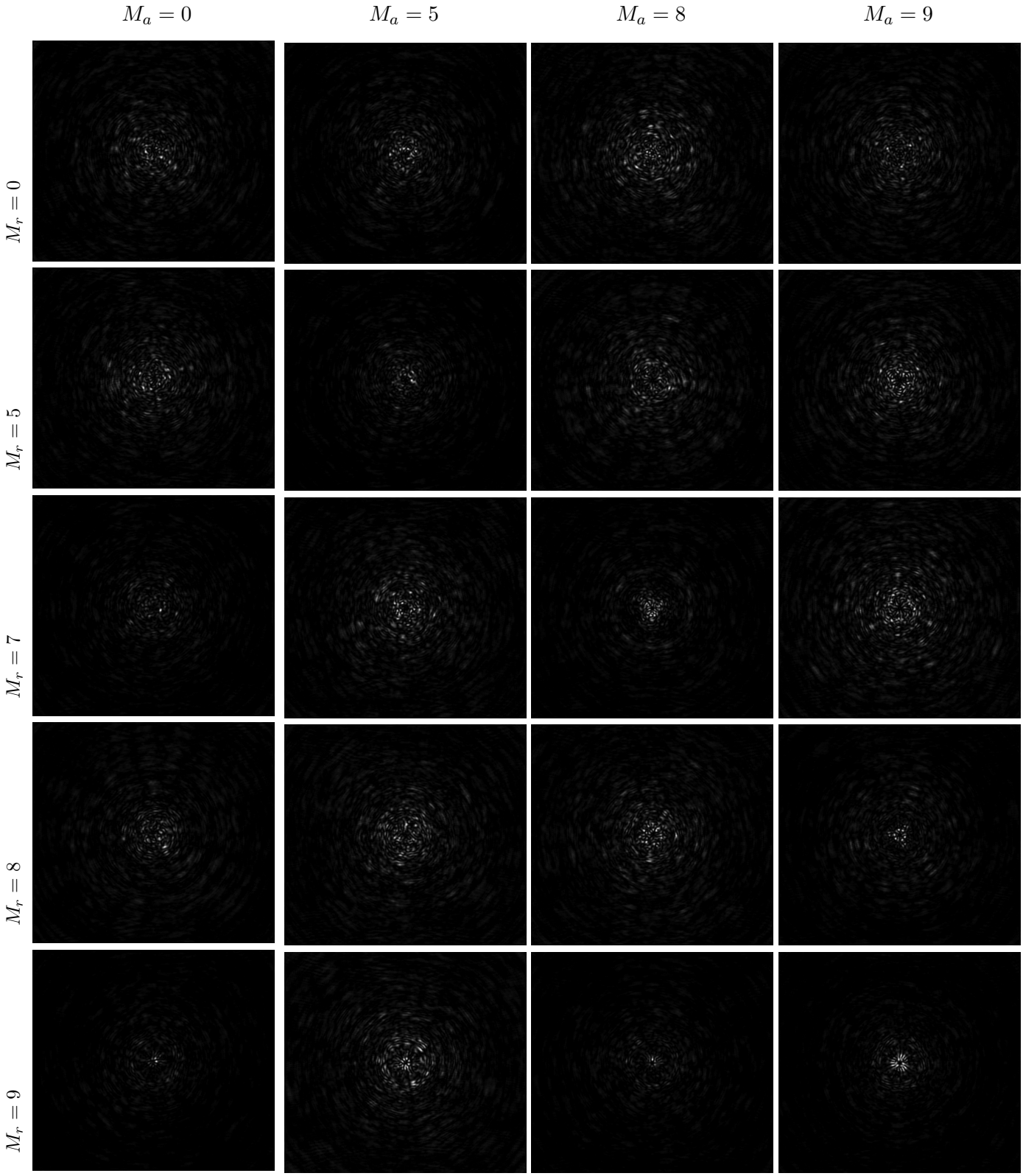

Fig. B.3: *Intensity profile of 1 realization for all studied azimuthal memory lengths and* $M_a = 0, 5, 8, 9$ *some representative cases of radial memory length* $M_z = 0, 3, 5, 8, 9$.

References

[1] I. Newton, *Opticks*. Great minds series, New York: Prometheus Books, 2003.

[2] C. Huygens, *Traité de la lumière, où sont expliquées les causes de ce qui luy arrive dans la réflexion, et dans la réfraction, et particulièrement dans l'étrange réfraction du cristal d'Islande: Avec un discours de la cause de la pesanteur*. Leiden: Pierre van der Aa, 1690.

[3] J. W. Goodman, *Introduction to Fourier Optics*. Englewood: Roberts & Co., 2005.

[4] G. Fowles, *Introduction to Modern Optics*. Dover Books on Physics Series, New York: Dover Publications, 1989.

[5] E. Hecht, *Optics*. London: Pearson, 5 ed., 2017.

[6] O. Darrigol, *A History of Optics from Greek Antiquity to the Nineteenth Century*. Oxford: OUP Oxford, 2012.

[7] M. Born and E. Wolf, *Principles of Optics: Electromagnetic Theory of Propagation, Interference and Diffraction of Light*. Amsterdam: Elsevier Science Limited, 6 ed., 1980.

[8] P. Rodgers, "The double-slit experiment," *Physics World*, vol. 15, pp. 15–15, sep 2002.

[9] W. Demtröder, *Experimentalphysik 2: Elektrizität und Optik*. Berlin: Springer-Verlag, 6 ed., 2013.

[10] A. S. F.R.S., "Ix. the elementary treatment of problems on the diffraction of light," *The London, Edinburgh, and Dublin Philosophical Magazine and Journal of Science*, vol. 31, no. 189, pp. 77–86, 1891.

[11] "Fresnel zone plate theory, generation, tolerancing, fabrication, and applications.." `http://zoneplate.lbl.gov/`. Accessed: 2019-10-30.

[12] J. W. Goodman and M. E. Cox, *Introduction to Fourier Optics*. Englewood: McGraw-Hill, 1968.

[13] C. J. Bouwkamp, "Diffraction theory," *Reports on Progress in Physics*, vol. 17, pp. 35–100, jan 1954.

[14] Éamon Lalor, "Conditions for the validity of the angular spectrum of plane waves∗," *J. Opt. Soc. Am.*, vol. 58, pp. 1235–1237, Sep 1968.

[15] J. Yang, J. Li, S. He, and L. V. Wang, "Angular-spectrum modeling of focusing light inside scattering media by optical phase conjugation," *Optica*, vol. 6, pp. 250–256, Mar 2019.

[16] T.-C. Poon and J.-P. Liu, *Introduction to Modern Digital Holography with MATLAB*. New York: Cambridge University Press, 2014.

[17] F. Dickey, T. Lizotte, S. Holswade, and D. Shealy, *Laser Beam Shaping Applications*. Optical Science and Engineering, Boca Raton: CRC Press, 2005.

[18] D. Gabor, "A new microscopic principle," *Nature*, vol. 161, no. 4098, pp. 777–778, 1948.

[19] H. Rubinsztein-Dunlop, A. Forbes, M. V. Berry, M. R. Dennis, D. L. Andrews, M. Mansuripur, C. Denz, C. Alpmann, P. Banzer, T. Bauer, E. Karimi, L. Marrucci, M. Padgett, M. Ritsch-Marte, N. M. Litchinitser, N. P. Bigelow, C. Rosales-Guzmán, A. Belmonte, J. P. Torres, T. W. Neely, M. Baker, R. Gordon, A. B. Stilgoe, J. Romero, A. G. White, R. Fickler, A. E. Willner, G. Xie, B. McMorran, and A. M. Weiner, "Roadmap on structured light," *Journal of Optics*, vol. 19, p. 013001, nov 2016.

[20] R. Horstmeyer, H. Ruan, and C. Yang, "Guidestar-assisted wavefront-shaping methods for focusing light into biological tissue," *Nature Photonics*, vol. 9, pp. 563 EP –, Aug 2015.

[21] A. E. Willner, H. Huang, Y. Yan, Y. Ren, N. Ahmed, G. Xie, C. Bao, L. Li, Y. Cao, Z. Zhao, J. Wang, M. P. J. Lavery, M. Tur, S. Ramachandran, A. F. Molisch, N. Ashrafi, and S. Ashrafi, "Optical communications using orbital angular momentum beams," *Adv. Opt. Photon.*, vol. 7, pp. 66–106, Mar 2015.

[22] J. T. Trauger and W. A. Traub, "A laboratory demonstration of the capability to image an earth-like extrasolar planet," *Nature*, vol. 446, no. 7137, pp. 771–773, 2007.

[23] H. Chen, Y. Gao, X. Liu, and Z. Zhou, "Imaging through scattering media using speckle pattern classification based support vector regression," *Opt. Express*, vol. 26, pp. 26663–26678, Oct 2018.

[24] J. Romero and M. Padgett, "Practical bound for dimensionality in high-dimensional entanglement," *Proceedings of the National Academy of Sciences*, vol. 111, no. 17, pp. 6122–6123, 2014.

[25] M. Dennis, K. O'Holleran, and M. Padgett, "Chapter 5 singular optics: Optical vortices and polarization singularities," *Progress in Optics*, vol. 53, pp. 293–363, 12 2009.

[26] C. Rosales-Guzmán and A. Forbes, *How to Shape Light with Spatial Light Modulators*. Bellingham: SPIE Press, 2017.

[27] Z. Zhang, Z. You, and D. Chu, "Fundamentals of phase-only liquid crystal on silicon (lcos) devices," *Light: Science &Amp; Applications*, vol. 3, pp. e213 EP –, Oct 2014.

[28] Hamamatsu, *Phase spatial light modulator LCOS-SLM*.

[29] I. M. Vellekoop and A. P. Mosk, "Focusing coherent light through opaque strongly scattering media," *Opt. Lett.*, vol. 32, pp. 2309–2311, Aug 2007.

[30] D. B. Conkey, A. M. Caravaca-Aguirre, and R. Piestun, "High-speed scattering medium characterization with application to focusing light through turbid media," *Opt. Express*, vol. 20, pp. 1733–1740, Jan 2012.

[31] P. Lai, L. Wang, J. W. Tay, and L. V. Wang, "Photoacoustically guided wavefront shaping for enhanced optical focusing in scattering media," *Nature Photonics*, vol. 9, pp. 126 EP –, Jan 2015.

[32] Y. Choi, T. Yang, C. Fang-Yen, P. Kang, K. Lee, R. Dasari, M. Feld, and W. Choi, "Overcoming the diffraction limit using multiple light scattering in a highly disordered medium," *Physical review letters*, vol. 107, p. 023902, 07 2011.

[33] M. Mounaix, D. Andreoli, H. Defienne, G. Volpe, O. Katz, S. Grésillon, and S. Gigan, "Spatiotemporal coherent control of light through a multiple scattering medium with the multispectral transmission matrix," *Phys. Rev. Lett.*, vol. 116, p. 253901, Jun 2016.

[34] S. M. Popoff, G. Lerosey, R. Carminati, M. Fink, A. C. Boccara, and S. Gigan, "Measuring the transmission matrix in optics: An approach to the study and control of light propagation in disordered media," *Phys. Rev. Lett.*, vol. 104, p. 100601, Mar 2010.

[35] A. Boniface, M. Mounaix, B. Blochet, R. Piestun, and S. Gigan, "Transmission-matrix-based point-spread-function engineering through a complex medium," *Optica*, vol. 4, pp. 54–59, Jan 2017.

[36] C.-L. Hsieh, Y. Pu, R. Grange, and D. Psaltis, "Digital phase conjugation of second harmonic radiation emitted by nanoparticles in turbid media," *Opt. Express*, vol. 18, pp. 12283–12290, Jun 2010.

[37] D. Wang, E. H. Zhou, J. Brake, H. Ruan, M. Jang, and C. Yang, "Focusing through dynamic tissue with millisecond digital optical phase conjugation," *Optica*, vol. 2, pp. 728–735, Aug 2015.

[38] M. Cui and C. Yang, "Implementation of a digital optical phase conjugation system and its application to study the robustness of turbidity suppression by phase conjugation," *Opt. Express*, vol. 18, pp. 3444–3455, Feb 2010.

[39] J. Yang, Y. Shen, Y. Liu, A. Hemphill, and L. Wang, "Focusing light through scattering media by polarization modulation based generalized digital optical phase conjugation," *Applied Physics Letters*, vol. 111, p. 201108, 11 2017.

[40] I. N. Papadopoulos, S. Farahi, C. Moser, and D. Psaltis, "Focusing and scanning light through a multimode optical fiber using digital phase conjugation," *Opt. Express*, vol. 20, pp. 10583–10590, May 2012.

[41] S. Tripathi, R. Paxman, T. Bifano, and K. C. Toussaint, "Vector transmission matrix for the polarization behavior of light propagation in highly scattering media," *Opt. Express*, vol. 20, pp. 16067–16076, Jul 2012.

[42] C. Ma, X. Xu, Y. Liu, and L. V. Wang, "Time-reversed adapted-perturbation (trap) optical focusing onto dynamic objects inside scattering media," *Nature Photonics*, vol. 8, pp. 931 EP –, Nov 2014.

[43] Y. M. Wang, B. Judkewitz, C. A. DiMarzio, and C. Yang, "Deep-tissue focal fluorescence imaging with digitally time-reversed ultrasound-encoded light," *Nature Communications*, vol. 3, no. 1, p. 928, 2012.

[44] K. Si, R. Fiolka, and M. Cui, "Fluorescence imaging beyond the ballistic regime by ultrasound-pulse-guided digital phase conjugation," *Nature Photonics*, vol. 6, no. 10, pp. 657–661, 2012.

[45] T. R. Hillman, T. Yamauchi, W. Choi, R. R. Dasari, M. S. Feld, Y. Park, and Z. Yaqoob, "Digital optical phase conjugation for delivering two-dimensional images through turbid media," *Scientific Reports*, vol. 3, pp. 1909 EP –, May 2013.

[46] B. Judkewitz, Y. M. Wang, R. Horstmeyer, A. Mathy, and C. Yang, "Speckle-scale focusing in the diffusive regime with time reversal of variance-encoded light (trove)," *Nature Photonics*, vol. 7, pp. 300 EP –, Mar 2013.

[47] J. Park, J.-H. Park, H. Yu, and Y. Park, "Focusing through turbid media by polarization modulation," *Opt. Lett.*, vol. 40, pp. 1667–1670, Apr 2015.

[48] R. Horisaki, R. Takagi, and J. Tanida, "Learning-based focusing through scattering media," *Appl. Opt.*, vol. 56, pp. 4358–4362, May 2017.

[49] M. I. Akhlaghi and A. Dogariu, "Tracking hidden objects using stochastic probing," *Optica*, vol. 4, pp. 447–453, Apr 2017.

[50] M. Rückel, J. Mack-Bucher, and W. Denk, "Adaptive wavefront correction in two-photon microscopy using coherence-gated wavefront sensing," *Proceedings of the National Academy of Sciences of the United States of America*, vol. 103, pp. 17137–42, 12 2006.

[51] D. Débarre, E. J. Botcherby, T. Watanabe, S. Srinivas, M. J. Booth, and T. Wilson, "Image-based adaptive optics for two-photon microscopy," *Opt. Lett.*, vol. 34, pp. 2495–2497, Aug 2009.

[52] E. R. Andresen, S. Sivankutty, V. Tsvirkun, G. Bouwmans, and H. Rigneault, "Ultrathin endoscopes based on multicore fibers and adaptive optics: a status review and perspectives," *Journal of Biomedical Optics*, vol. 21, no. 12, pp. 1 – 12, 2016.

[53] O. Katz, E. Small, and Y. Silberberg, "Looking around corners and through thin turbid layers in real time with scattered incoherent light," *Nature Photonics*, vol. 6, no. 8, pp. 549–553, 2012.

[54] Y. Choi, C. Yoon, M. Kim, W. Choi, and W. Choi, "Optical imaging with the use of a scattering lens," *IEEE Journal of Selected Topics in Quantum Electronics*, vol. 20, pp. 61–73, March 2014.

[55] T. Cizmár, M. Mazilu, and K. Dholakia, "In situ wavefront correction and its application to micromanipulation," *Nature Photonics*, vol. 4, no. 6, pp. 388–394, 2010.

[56] S. Bianchi and R. Di Leonardo, "A multi-mode fiber probe for holographic micromanipulation and microscopy," *Lab Chip*, vol. 12, pp. 635–639, 2012.

[57] K. Deisseroth, "Optogenetics," *Nature Methods*, vol. 8, no. 1, pp. 26–29, 2011.

[58] F. Dickey, *Laser Beam Shaping: Theory and Techniques, Second Edition*. Boca Raton: CRC Press, 2018.

[59] A. Daniel, L. Liberman, and Y. Silberberg, "Wavefront shaping for glare reduction," *Optica*, vol. 3, pp. 1104–1106, Oct 2016.

[60] G. J. Gbur, *Gregory J. Gbur*. Boca Raton: CRC Press, 2016.

[61] J. Nye and M. V. Berry, "Dislocations in wave trains," *Proc. R. Soc. Lond. A.*, vol. 336, pp. 165–190, 01 1974.

[62] I. Freund, "Optical vortices in gaussian random wave fields: statistical probability densities," *J. Opt. Soc. Am. A*, vol. 11, pp. 1644–1652, May 1994.

[63] L. D. Angelis, T. Bauer, F. Alpeggiani, and L. Kuipers, "Index-symmetry breaking of polarization vortices in 2d random vector waves," *Optica*, vol. 6, pp. 1237–1243, Sep 2019.

[64] J. Masajada and B. Dubik, "Optical vortex generation by three plane wave interference," *Opt. Commun.*, vol. 198, pp. 21–27, 10 2001.

[65] J. Wang and A. Z. Genack, "Transport through modes in random media," *Nature*, vol. 471, no. 7338, pp. 345–348, 2011.

[66] A. Z. Genack and A. A. Chabanov, "Signatures of photon localization," *Journal of Physics A: Mathematical and General*, vol. 38, pp. 10465–10488, nov 2005.

[67] T. Strudley, T. Zehender, C. Blejean, E. P. A. M. Bakkers, and O. L. Muskens, "Mesoscopic light transport by very strong collective multiple scattering in nanowire mats," *Nature Photonics*, vol. 7, no. 5, pp. 413–418, 2013.

[68] D. J. Pine, D. A. Weitz, P. M. Chaikin, and E. Herbolzheimer, "Diffusing wave spectroscopy," *Phys. Rev. Lett.*, vol. 60, pp. 1134–1137, Mar 1988.

[69] F. Scheffold and G. Maret, "Universal conductance fluctuations of light," *Phys. Rev. Lett.*, vol. 81, pp. 5800–5803, Dec 1998.

[70] W. Langbein, J. M. Hvam, and R. Zimmermann, "Time-resolved speckle analysis: A new approach to coherence and dephasing of optical excitations in solids," *Phys. Rev. Lett.*, vol. 82, pp. 1040–1043, Feb 1999.

[71] F. Ferri, D. Magatti, A. Gatti, M. Bache, E. Brambilla, and L. A. Lugiato, "High-resolution ghost image and ghost diffraction experiments with thermal light," *Phys. Rev. Lett.*, vol. 94, p. 183602, May 2005.

[72] T. Schwartz, G. Bartal, S. Fishman, and M. Segev, "Transport and anderson localization in disordered two-dimensional photonic lattices," *Nature*, vol. 446, no. 7131, pp. 52–55, 2007.

[73] Y. Bromberg and H. Cao, "Generating non-rayleigh speckles with tailored intensity statistics," *Phys. Rev. Lett.*, vol. 112, p. 213904, May 2014.

[74] D. D. Battista, D. Ancora, G. Zacharakis, G. Ruocco, and M. Leonetti, "Hyperuniformity in amorphous speckle patterns," *Opt. Express*, vol. 26, pp. 15594–15608, Jun 2018.

[75] J. W. Goodman, "Some fundamental properties of speckle∗," *J. Opt. Soc. Am.*, vol. 66, pp. 1145–1150, Nov 1976.

[76] N. Bender, H. Yilmaz, Y. Bromberg, and H. Cao, "Customizing speckle intensity statistics," *Optica*, vol. 5, pp. 595–600, May 2018.

[77] D. Di Battista, D. Ancora, M. Leonetti, and G. Zacharakis, "Tailoring non-diffractive beams from amorphous light speckles," *Applied Physics Letters*, vol. 109, p. 121110, 09 2016.

[78] R. Fischer, I. Vidal, D. Gilboa, R. R. Correia, A. C. Ribeiro-Teixeira, S. D. Prado, J. Hickman, and Y. Silberberg, "Light with tunable non-markovian phase imprint," *Physical Review Letters*, vol. 115, Aug 2015.

[79] T. Eichelkraut and A. Szameit, "Random sudoku light," *Nature*, vol. 526, pp. 643 EP –, Oct 2015.

[80] A. A. Markov, "Rasprostranenie zakona bol'shih chisel na velichiny, zavisyaschie drug ot druga," *Izvestiya Fiziko-matematicheskogo obschestva pri Kazanskom universitete*, vol. 15, pp. 135–156, 1906.

[81] A. Mura, *Non-Markovian Stochastic Processes and their Applications: from Anomalous Diffusion to Time Series Analysis.* PhD thesis, Università di Bologna, 2008.

[82] A. Chiuri, C. Greganti, L. Mazzola, M. Paternostro, and P. Mataloni, "Linear optics simulation of quantum non-markovian dynamics," *Scientific Reports*, vol. 2, pp. 968 EP –, Dec 2012.

[83] B.-H. Liu, L. Li, Y.-F. Huang, C.-F. Li, G.-C. Guo, E.-M. Laine, H.-P. Breuer, and J. Piilo, "Experimental control of the transition from markovian to non-markovian dynamics of open quantum systems," *Nature Physics*, vol. 7, no. 12, pp. 931–934, 2011.

[84] J. Cho, S. Bose, and M. S. Kim, "Optical pumping into many-body entanglement," *Phys. Rev. Lett.*, vol. 106, p. 020504, Jan 2011.

[85] J. T. Barreiro, M. Müller, P. Schindler, D. Nigg, T. Monz, M. Chwalla, M. Hennrich, C. F. Roos, P. Zoller, and R. Blatt, "An open-system quantum simulator with trapped ions," *Nature*, vol. 470, no. 7335, pp. 486–491, 2011.

[86] M. Paternostro, D. Vitali, S. Gigan, M. Kim, C. Brukner, J. Eisert, and M. Aspelmeyer, "Creating and probing multipartite macroscopic entanglement with light," *Physical review letters*, vol. 99, p. 250401, 01 2008.

[87] J. M. Dudley, F. Dias, M. Erkintalo, and G. Genty, "Instabilities, breathers and rogue waves in optics," *Nature Photonics*, vol. 8, Sep 2014.

[88] D. R. Solli, C. Ropers, P. Koonath, and B. Jalali, "Optical rogue waves," *Nature*, vol. 450, no. 7172, 2007.